IOP Publishing

Magnetic Excitations and Geometric Confinement

Theory and simulations

Gary Matthew Wysin

Chapter 8

Vortices in layered or 2D ferromagnets

Many magnetic crystals have an anisotropic structure that is layered and, hence, the magnetic interactions have a 2D anisotropy. Then, the dynamics is close to that of independent planes of magnetic ions, i.e. 2D magnets. Depending on the details of the magnetic interactions, different types of topological excitations are possible, known both as solitons and vortices. In this chapter the structure of the two types of vortices in ferromagnets is presented. The unbinding of vortices in particle–anti-particle pairs produces the Berezinskii–Kosterlitz–Thouless (BKT) topological phase transition. The transition can be studied using Monte Carlo (MC) and spin dynamics (SD) simulations. An ideal gas of vortices is discussed as a model for their contribution to the thermodynamics. Some simulations of the dynamic correlations in the ferromagnetic (FM) XY model are presented to show the changes in dynamic correlations with temperature and wave vector.

8.1 A 2D ferromagnet with easy-plane exchange anisotropy

In this chapter we consider a model of three-component spins occupying the sites of some 2D lattice, with a FM nearest neighbor interaction. The model applies to materials such as K_2CuF_4 [1, 2], where the magnetic ions occupy well-defined layers in a crystal, separated by larger spacing than the intra-layer nearest neighbor distance. Then, the spin interactions are quasi-2D; for the most part we ignore the inter-layer couplings. It can be kept in mind that although the inter-layer couplings are small, at low enough temperature they can be considered important, where they lead to 3D ordering. The model is considered above any 3D ordering temperature. Much of the analysis can be performed assuming a square lattice; the analysis and certain results have some dependencies on the particular lattice, however, the basic physics effects are the same.

doi:10.1088/978-0-7503-1074-1ch8

A model Hamiltonian is assumed with XXZ symmetry as in (1.45), and defining the in-plane exchange constant as $J^x = J$, and the out-of-plane exchange constant as

$$J^z = \lambda J^x, \quad 0 \leqslant \lambda < 1, \tag{8.1}$$

the Hamiltonian, with only nearest neighbor interactions, is taken as

$$H = -J \sum_{(i,j)} \left(S_i^x S_j^x + S_i^y S_j^y + \lambda S_i^z S_j^z - S^2 \right). \tag{8.2}$$

The sum is over nearest neighbor pairs of sites (i, j), which could occupy a square, triangular, hexagonal, or other 2D lattice. The last factor of S^2 forces the ground state energy to be zero. The usual XY model is the limit $\lambda = 0$. At $\lambda \to 1$ the interaction becomes isotropic; this isotropic Heisenberg limit is outside the discussion in this chapter. It is important for the considerations here to include at least an infinitesimal XY or easy-plane anisotropy. By including the anisotropy parameter λ, the properties of vortices and the BKT vortex-unbinding transition can be found to change with anisotropy strength. Besides, the exchange interactions in real quasi-2D materials may be very close to isotropic, with only weak easy-plane character ($\lambda \approx 0.99$ for K_2CuF_4 [1, 2]). This model does not include the plane rotor (PR) model (two-component spins). By using three-component spins, the model has true SD without the need for introducing an inertia as in the rotor model. In this chapter only FM coupling is assumed, and the demagnetization field is neglected.

The Hamiltonian (8.2) has already been discussed concerning MC simulations (equation (4.137)) and the discrete SD equations of motion, for the in-plane angle ϕ_i and out-of-plane spin component S_i^z, were found in (5.23) and (5.24). Using $S_i^z = S \sin\theta_i$ in planar spherical coordinates, the dynamics can alternatively be set in terms of the out-of-plane angles θ_i. This Hamiltonian is a combination of an isotropic part ($-J\mathbf{S}_i \cdot \mathbf{S}_j$ pair interactions) and an anisotropy term,

$$H_{\text{ani}} = +J\delta \sum_{(i,j)} S_i^z S_j^z, \quad \text{where } \delta \equiv 1 - \lambda. \tag{8.3}$$

For much of the analysis, a continuum description is useful. The continuum isotropic Hamiltonian has been developed in chapter 2, see in particular (2.57) for an isotropic chain, (2.28) for a square lattice and (2.33) for arbitrary lattices. We suppose that the original discrete system is defined on a square lattice. Letting $S_i^z \to S^z(\mathbf{r})$ and $S_j^z \to S^z(\mathbf{r} + \mathbf{a}_j)$, it is straightforward to expand this anisotropic part and arrive at the total continuum limit Hamiltonian that was derived from interactions on a square lattice (four nearest neighbors $\mathbf{a}_j = \pm a\hat{\mathbf{x}}, \pm a\hat{\mathbf{y}}$):

$$H = \frac{1}{2} JS^2 \int \mathrm{d}^2 r \left\{ \left(1 - \delta \cos^2\theta\right) |\nabla\theta|^2 + \cos^2\theta |\nabla\phi|^2 + 4\delta \sin^2\theta \right\}. \tag{8.4}$$

In this chapter lengths such as r are assumed to be in units of the lattice constant a.

Exercise 8.1. Verify that Hamiltonian (8.4) results from taking a continuum limit of (8.2) on a square lattice. The isotropic part is the 1D to 2D generalization of (2.57), which should be included with the anisotropic part from (8.3).

A Hamiltonian similar to (8.4) was developed and the equations of motion analyzed by Hikami and Tsuneto [1], but with half the strength on the term $4\delta \sin^2\theta$. Either by the techniques of chapter 2 or by the continuum limits of (5.23) and (5.24), one arrives at the dynamical equations (see also the work of Gouvêa *et al* [3] and Wysin *et al* [4]),

$$(JS)^{-1}\dot{\phi}\cos\theta = \left[2\delta - \frac{1}{2}(\delta\ |\nabla\theta|^2 + |\nabla\phi|^2)\right]\sin 2\theta - \left(1 - \delta\cos^2\theta\right)\nabla^2\theta \qquad (8.5a)$$

$$(JS)^{-1}\dot{\theta} = \cos\theta\ \nabla^2\phi - 2\sin\theta\nabla\theta\cdot\nabla\phi. \qquad (8.5b)$$

Exercise 8.2. Verify that the dynamical equations (8.5) result from the continuum Hamiltonian (8.4), for instance, by using functional derivatives (2.129) as described in chapter 2, and then finding the dynamics from (2.103).

Takeno and Homma [5] also arrived at equivalent dynamic equations, using different notation, but mainly analyzed them for a 1D model. Nikiforov and Sonin [6] considered a similar Hamiltonian but with the anisotropy inserted in a local interaction form, $+J\delta(S_i^z)^2$. This does not make a strong difference in the vortex structures that result or the basic physics, beyond some rescaling of parameters. The first step in the subsequent analysis will be to describe the kinds of vortex solutions, both static and dynamic, that are possible from these equations.

After describing the basic vortex structures (the spin waves present were described in chapter 6), the role played by vortices in the BKT topological transition will be described. Dynamics of vortices can be seen in the dynamic correlations above the BKT transition temperature, although this response is mixed in with a similar response due to spin waves. There is also considerable interest in the particular interaction between an individual vortex and the surrounding bath of spin waves.

8.2 In-plane and out-of-plane vortices

One can seek the static vortex solutions of (8.5), putting $\dot{\phi} = \dot{\theta} = 0$. Then (8.5*b*) has solutions of a form where $\phi = \phi(\varphi)$ depends only on azimuthal position coordinate φ and $\theta = \theta(r)$ depends only on radial position coordinate r, both measured relative

to an arbitrary center, which is taken as the origin for now. This means $\nabla\phi \cdot \nabla\theta = 0$, and then (8.5*b*) becomes a 2D Laplace equation for the in-plane angle:

$$\nabla^2\phi = 0. \tag{8.6}$$

Using either circular coordinates (r, φ) or Cartesian coordinates (x, y), the in-plane angle for a vortex solution is

$$\phi = q\varphi + \phi_0 = q\,\tan^{-1}\left(\frac{y}{x}\right) + \phi_0. \tag{8.7}$$

$q = \pm 1, \pm 2, \ldots$ is the *vorticity charge* or vorticity for short, and ϕ_0 is a constant of integration or *phase angle* that gives the direction of the spin field on the positive x-axis. For example, with $\phi_0 = \pi/2$, the spins point in the counterclockwise sense (for $q = +1$) as one moves along a path around the origin. The solutions are called vortices ($q = +1, +2, \ldots$) or anti-vortices ($q = -1, -2, \ldots$) according to the sign of q. A vortex solution has a gradient given by

$$\nabla\phi = \frac{1}{r}\frac{\partial\phi}{\partial\varphi}\hat{\boldsymbol{\varphi}} = \frac{q}{r}\hat{\boldsymbol{\varphi}}, \tag{8.8}$$

where the azimuthal unit vector is

$$\hat{\boldsymbol{\varphi}} = \hat{\mathbf{z}} \times \hat{\mathbf{r}} = -\hat{\mathbf{x}}\sin\varphi + \hat{\mathbf{y}}\cos\varphi = (-\sin\varphi, \cos\varphi). \tag{8.9}$$

At the origin there is a singularity; it might be referred to as the *vortex core*. The field $\nabla\phi$ is analogous to the magnetic induction around an infinitely thin current-carrying wire[1]. There is a corresponding Ampere's law for the total vorticity charge enclosed within a path surrounding the vortex core:

$$\oint \nabla\phi \cdot \mathrm{d}\ell = 2\pi q. \tag{8.10}$$

Although the in-plane angle for an individual vortex satisfies a 2D Laplace equation, the gradient can be rotated 90° to the radial direction by forming the object $\nabla\phi \times \hat{\mathbf{z}} = (q/r)\hat{\mathbf{r}}$. This is like the 2D electric field of a line of charge. This implies a 2D Poisson equation for that situation, corresponding to Gauss's Law,

$$\nabla \cdot (\nabla\phi \times \hat{\mathbf{z}}) = 2\pi q\ \delta(\mathbf{r}). \tag{8.11}$$

Also with the identity,

$$\nabla \cdot (\nabla\phi \times \hat{\mathbf{z}}) = \hat{\mathbf{z}} \cdot (\nabla \times \nabla\phi) \tag{8.12}$$

(or via Stokes' theorem), one can see that an Ampere's law equation holds,

$$\nabla \times \nabla\phi = 2\pi q\ \delta(\mathbf{r})\hat{\mathbf{z}}. \tag{8.13}$$

Although evaluated here for an individual vortex, one can see by superposition that (8.10) applies to any number of enclosed vortices, if q on the right-hand side is the

[1] A real current-carrying wire has no true singularity in its field because the current must be spread out over some cross-section. In the same way, there is no true singularity in the spin field of the original model on a lattice. The singularity appeared only as a result of the continuum limit from a discrete system.

algebraic sum of their vorticity charges. If the path of integration encloses a vortex and the opposite signed anti-vortex, this integral will be zero. This already shows that the vorticity charge follows a topological conservation law. Vortices can only be created into a system if the total vorticity generated through any process does not change. Every vortex created (in a closed system) must be balanced by a corresponding anti-vortex. In an open system, vortices or anti-vortices can enter or leave at the edges, and total vorticity charge is not conserved.

8.2.1 In-plane vortices

The vortex type is determined by the structure of the out-of-plane angle. Equation (8.5*a*) in the static limit has been found both from analytics [1, 5] and numerics [3, 4] to have two types of solutions. The first is the *planar vortex* or *in-plane vortex* solution, where all spins remain in the xy-plane:

$$\theta_{\rm ip} = 0. \tag{8.14}$$

In this case, the only contribution to the energy is from that associated with $|\nabla\phi|^2$,

$$E_{\rm ip} = \frac{1}{2}JS^2 \int {\rm d}^2 r\ |\nabla\phi|^2 = \frac{1}{2}JS^2 \int_0^{2\pi} {\rm d}\varphi \int_{r_0}^{R} r\ {\rm d}r\ \frac{q^2}{r^2} = \pi JS^2 q^2 \ln\frac{R}{r_0}. \tag{8.15}$$

To make the result finite, a short-distance cutoff r_0, of the order of a lattice spacing, is applied. In addition, the large radius integration is cutoff at some upper limit R, which is of the order of the system size. The individual, perfect vortex, therefore, would have a weakly divergent energy in an infinite system. Estimates of the single in-plane vortex energy on a square lattice ([7], figure 6) in circular systems of varying radius R, give the same mathematical form as (8.15), but with π replaced by $\tilde{\pi} = 3.06$ and the cutoff distance $r_0 = 0.24a$, where a is the lattice spacing. In practice, the more important energetic result would be the total energy of a vortex–anti-vortex (VA) pair. It is an interesting exercise to show that the energy of a VA pair, separated by some distance R, takes a similar form[2], see the derivation of (9.118).

8.2.2 Out-of-plane vortices

There is a second type of vortex solution, the *out-of-plane vortex*, with non-zero θ that is maximum at the vortex core position, and decays away exponentially far away. Consider (8.5*a*) at small radius, where by symmetry only one of the values $\theta \approx p\pi/2$ is assumed, with $p = \pm 1$ being the *core polarization*. Expanding as $\theta \approx p\pi/2 + \epsilon$, with $\epsilon \ll 1$, and keeping the leading terms in ϵ, one obtains

$$-\left(4\delta - \frac{q^2}{r^2}\right)\epsilon - \left(\frac{{\rm d}^2\epsilon}{{\rm d}r^2} + \frac{1}{r}\frac{{\rm d}\epsilon}{{\rm d}r}\right) = 0. \tag{8.16}$$

Terms that were cubic in ϵ have been dropped. This allows for a power law solution of the form $\epsilon = r^n$. For small enough r, the term involving 4δ can be ignored relative

[2] Refer to a pair of long straight wires separated by distance R and carrying electric currents in opposite directions. The energy stored in their magnetic field is also finite and depends on $\ln R$.

to the others, which leads to the power being $n = |q|$. For large r, the asymptotics requires $\theta \to 0$ and the solution needs to obey the leading terms,

$$4\delta \cdot \theta - (1 - \delta)\left(\frac{\mathrm{d}^2\theta}{\mathrm{d}r^2} + \frac{1}{r}\frac{\mathrm{d}\theta}{\mathrm{d}r}\right) = 0. \tag{8.17}$$

This has an exponential behavior with the exponent determined by the ratio $4\delta/(1 - \delta)$. This gives the length scale of the far field, r_v, which is known as the *vortex core radius*,

$$r_\mathrm{v} \equiv \frac{1}{2}\sqrt{\frac{1 - \delta}{\delta}} = \frac{1}{2}\sqrt{\frac{\lambda}{1 - \lambda}}. \tag{8.18}$$

Then, Gouvêa *et al* [3] determined the asymptotic form for the out-of-plane structure in an out-of-plane vortex, in which we include the core polarization $p = \pm 1$ and the possibility of $|q| \geqslant 1$,

$$\theta_\mathrm{oop} \approx p\left[\frac{\pi}{2} - A_0\left(\frac{r}{r_\mathrm{v}}\right)^{|q|}\right], \quad r \to 0 \tag{8.19a}$$

$$\theta_\mathrm{oop} \approx pA_\infty\sqrt{\frac{r_\mathrm{v}}{r}}\,\mathrm{e}^{-r/r_\mathrm{v}}, \quad r \to \infty. \tag{8.19b}$$

Parameters $A_0 = 3\pi/10$ and $A_\infty = \pi\mathrm{e}/5$ are constants that are determined by matching these two solutions at the radius $r = r_\mathrm{v}$. This is an approximate analysis, as there is no analytic solution known for all r. For the compound K_2CuF_4 with $\lambda \approx 0.99$, the core radius is $r_\mathrm{v} \approx 5$, in lattice constants. That means the discreteness effects of the underlying lattice may not be too strong, and the continuum description should be acceptable. Note, however, there is not a corresponding length scale for the in-plane vortex solution.

The energy of the out-of-plane vortex can be evaluated approximately from this asymptotic solution. In [3] it is estimated that the out-of-plane vortex energy E_oop is greater than E_ip when $\lambda \ll 0.8$; conversely, E_oop is lower than E_ip for values of λ closer to 1. This is an indication of their ranges of stability, which is discussed below in section 8.3.

8.2.3 Discrete lattice vortex solutions

Static in-plane or out-of-plane vortex solutions on a lattice can be found numerically. They may be close to the approximate analytic solutions already described, such as (8.7) for the in-plane angle, and (8.19) for the out-of-plane component if $\lambda > \lambda_\mathrm{c}$. These become modified slightly on a grid. To obtain the correct solution on a grid, start by setting the in-plane angles ϕ_n according to (8.7), for the vortex centered in the system. For instance, if an in-plane vortex is assumed, one can show from the equations of motion such as (2.103) that the static in-plane angles must satisfy

$$\sum_{(j)} \sin\left(\phi_i - \phi_j\right) = 0. \tag{8.20}$$

This must hold at all sites i, summing over the nearest neighbors j, indicated by (j). Most sites have z nearest neighbors, where z is the coordination number of the lattice. The sites at the boundary of the system have a few fewer neighbors. The equation is analogous to $\nabla^2\phi = 0$ for the continuum problem. In the core region, the discrete and continuum problems give slight differences in the structure.

The discrete structure can be calculated numerically by the spin alignment technique described earlier in section 3.5.1. To do so, one uses the effective field $\mathcal{F}_i$ that acts on the spin at site i, as defined in (5.3). Referring also to (5.4), the static vortex structure is obtained when each spin is parallel to its field $\mathcal{F}_i$, leading to

$$\dot{\mathbf{S}}_i = \mathbf{S}_i \times \left[\mathcal{F}_i - \frac{\alpha}{S}\left(\mathbf{S}_i \times \mathcal{F}_i\right) \right] = 0. \tag{8.21}$$

The spin alignment algorithm iteratively sets each unit spin to be in the direction of its current $\mathcal{F}_i$, starting from some initial state. To be completely general, it is best to initiate the system also with some small out-of-plane spin components, breaking the planar symmetry numerically. This allows for the generation of an organized out-of-plane structure for the cases where that is the most stable vortex. Conversely, if the in-plane vortex is the more stable one, any initial out-of-plane structure will decay away under the iteration. The process is repeated until the structural changes are less than some desired precision. The stopping criterion could be based on the overall changes in spin components, or on the changes in the total energy, or both, see section 3.5.1. Indeed, any method that relaxes into the locally lowest energy configuration is acceptable.

Profiles of $S^z(r)$ as obtained by spin alignment relaxation are given in figure 8.1 for some different values of $\lambda > \lambda_c$, on a circular system of radius $R = 15a$ using a square lattice grid (lattice constant a). A strong demagnetization boundary condition was used in the spin alignment relaxation, setting the spins on the circular edge of the system to remain in the xy-plane and follow the circular boundary. The approximate solution (8.19a) for $r < r_v$ is shown as solid curves; the corresponding solution (8.19b) for $r > r_v$ is indicated with dotted curves. Note that the point $r = r_v$ always gives the value $\theta = \pi/5$ for the analytic solution, marked with an arrow on the plot. The comparison to the approximate analytic solution (8.19) is reasonable but not particularly good, probably because of the linearization used to arrive at that solution. In addition, the asymptotic solutions do not take into account some rearrangement of the in-plane angles in the core region on the discrete lattice.

8.3 Vortex instability

One can note that for $\lambda = 0$ (the XY limit), the vortex core radius for an out-of-plane vortex becomes $r_v = 0$. This would imply that there is no far field asymptotic region. The validity of the continuum limit to obtain that solution also might be questionable. One can note that $\lambda = 0.80$ gives $r_v = 1$, and $\lambda = 2/3$ gives $r_v = 1/\sqrt{2}$. One might expect that a vortex core radius near these values would be the limit where the continuum description must be strongly corrected by lattice discreteness effects. In fact, these effects cause an instability of both vortex types.

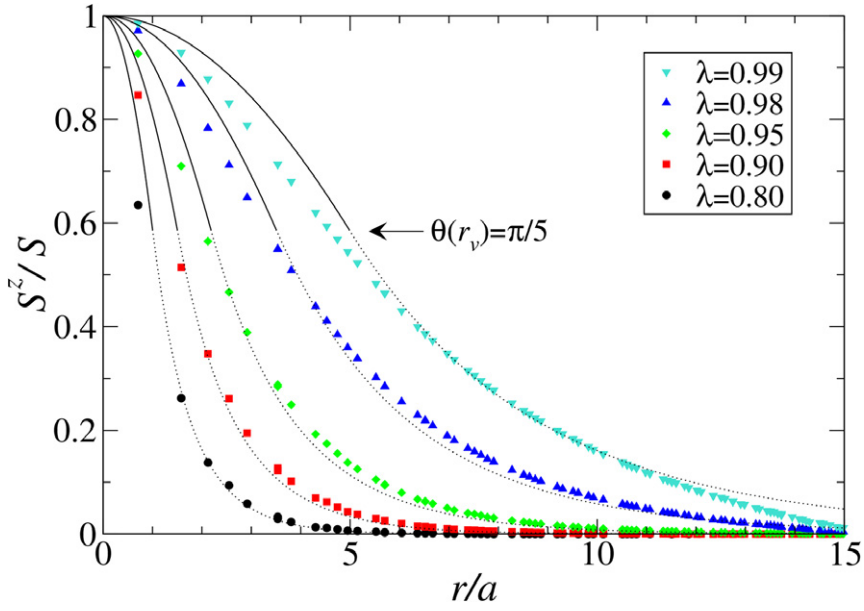

Figure 8.1. Out-of-plane vortex structure as seen in the out-of-plane spin component S^z as a function of radius from the vortex center, for indicated anisotropy constants $\lambda > \lambda_c$. Symbols were obtained by the spin alignment numerical relaxation calculations for a circular system of radius $R = 15a$, discretized on a square lattice. The solid curves are asymptotic expression (8.19*a*) for $r < r_v$; dotted curves are asymptotic expression (8.19*b*) for $r > r_v$. The curves connect at $r = r_v$, indicated with the arrow. Note how the results for $\lambda = 0.99$ have been limited by the Dirichlet ($S_z(R) = 0$) strong demagnetization boundary condition that was applied.

8.3.1 Numerical simulations for stability

The vortex stability can be tested by numerical simulations for the vortices on a lattice. The approach was carried out by Wysin *et al* [3, 4], integrating the discrete equations of motion (5.4) written in terms of Cartesian coordinates, including Landau–Lifshitz–Gilbert damping and using unit length spins $\mathbf{s}_i$,

$$\dot{\mathbf{s}}_i = \mathbf{s}_i \times \mathcal{F}_i - \alpha \mathbf{s}_i \times (\mathbf{s}_i \times \mathcal{F}_i) \tag{8.22a}$$

$$\mathcal{F}_i = -\frac{\partial H}{\partial \mathbf{S}_i} = JS \sum_{(i,j)} \left(s_j^x \hat{\mathbf{x}} + s_j^y \hat{\mathbf{y}} + \lambda s_j^z \hat{\mathbf{z}} \right). \tag{8.22b}$$

The sum for $\mathcal{F}_i$ contains only the nearest neighbor sites j. A damping parameter $\alpha = 0.1$ can be used to allow the system to seek energetically stable configurations. The equations can be integrated forward in time by any good method, such as fourth-order Runge–Kutta (RK4), provided one checks energy conservation for $\alpha = 0$. RK4 with a time step of $\Delta t = 0.04$ in units of $(JS)^{-1}$ works fairly well. A system on a square lattice as small as 40×40, with open boundaries, is sufficient to test vortex stability.

For these simulations, the initial condition for the in-plane angle is the planar vortex structure, equation (8.7). For the initial out-of-plane component s_i^z, one can check whether the system prefers the in-plane of out-of-plane structure by starting from some non-zero values. The obvious choices are 1) set all s_i^z to the same initial small constant $z_0 \ll 1$ and 2) set the initial s_i^z to a narrow distribution of random values with zero mean, which adds some small non-zero fluctuations, breaking the symmetry. In the first choice, if the out-of-plane vortex is more stable, the system will grow the s^z profile until it becomes an out-of-plane vortex profile with core polarization p the same sign as z_0. In the second choice, if the out-of-plane vortex is more stable, it could emerge with either sign of polarization. For both methods, if the planar vortex is more stable, it will emerge. The process can be carried out for a sequence of values of λ, thus mapping out the stability region of both vortex types. One can also make simulations with an approximate out-of-plane vortex initial condition, based on the asymptotic solution (8.19). Usually the vortex stability can be decided already by observing the simulation out to an integration time of $t = 100(JS)^{-1}$.

The results of this type of study are simple, although they can depend on the final time of the integration. For $\lambda < 0.72 \pm 0.01$, the vortex structure evolves towards the planar configuration, with $s_i^z \approx 0$ for all sites, and especially for those at the vortex core. On the other hand, for $\lambda > 0.72 \pm 0.01$, a non-zero s_i^z profile emerges, with its maximum at the vortex core, and decaying away as a function of the radius, similar to the asymptotic form found above. This is the stable out-of-plane vortex. This shows that there is a *critical anisotropy constant* $\lambda_c \approx 0.72 \pm 0.01$ at which the stability of each vortex type is destroyed, and the other type becomes the stable structure. There is an uncertainty of the order of ± 0.01 for a fairly simple reason: when $\lambda \approx \lambda_c$, the time scales of the evolution become longer. Only with fairly extended integrations in this region is it possible to accurately decide which type is more stable.

These vortex stability simulations can also be done on triangular ($z = 6$ nearest neighbors) and hexagonal ($z = 3$ nearest neighbors). One finds $\lambda_c \approx 0.62$ for the triangular lattice and $\lambda_c \approx 0.86$ for the hexagonal lattice. This suggests that a greater coordination number (more interactions) leads to greater stability of the planar vortex. This can be tested by some analysis of the spin energetics in the vortex core, described next.

8.3.2 Discrete energetics of vortex core stability

An analytic stability analysis of the vortex solutions is difficult to do in the continuum limit, because of the singularity at the vortex core. The continuum evaluation of vortex energy is not well defined and requires a cutoff. However, the energy should have a very specific value on the original lattice being considered. This leads one to consider an analysis of the vortex structure and energy in the core region, on the lattice as carried out in [8].

The approach is the following. Consider a vortex centered in one cell on a square lattice, see 8.2 for the notation. The in-plane spin structure is taken to follow (8.7),

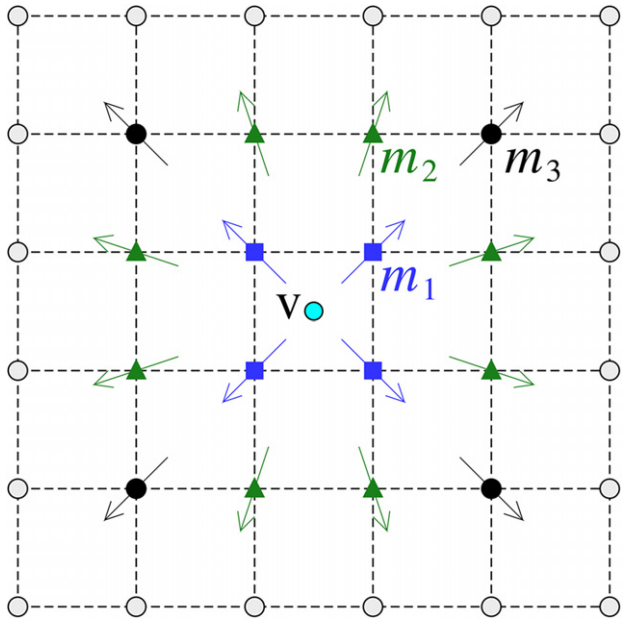

Figure 8.2. Notation for the spins sites with different out-of-plane spin components s^z around a $q = 1$ vortex centered at point v. There are four sites (blue squares) at radius $r_1 = \sqrt{1/2}$ with $s^z = m_1$, eight sites (green triangles) at radius $r_2 = \sqrt{5/2}$ with $s^z = m_2$ and four sites (black dots) at radius $r_3 = \sqrt{9/2}$ with $s^z = m_3$. In the outer surroundings $s^z = 0$ is assumed (gray dots). The in-plane spin directions follow (8.7) with $\phi_0 = 0$.

with the vortex at the origin, and with $q = 1$ and $\phi_0 = 0$. The out-of-plane spin components s_i^z are set to discrete values m_1, m_2, m_3, *etc*, symmetrically around the vortex center, according to increasing radius of the sites from the vortex center. All sites at the same radius are assigned the same value of m. Assuming this circularly symmetric arrangement, one can evaluate the Hamiltonian and write out the vortex energy-dependence on m_j, $j = 1, 2, 3 \ldots$, where j labels the radii r_j. A minimization of the total energy so obtained on the original lattice can reveal the energetic stability limits.

This procedure can be carried out first letting only the sites nearest to the core have non-zero out-of-plane component m_1, and all others $m_j = 0$. The four spins nearest the central core occupy at radius $r_1 = \sqrt{1/2}$ and have in-plane angles 45°, 135°, 225°, 315°, and their in-plane components are reduced by the factor $\cos\theta = (1 - m_1^2)^{1/2}$ due to their out-of-plane tilting. The differences of their in-plane angles are $\pm 90°$, so those four exchange bonds contribute an amount $4JS^2(1 - \lambda m_1^2)$ to the energy (above the ground state). There are also eight bonds connecting outward to the next eight sites at radius $r_2 = \sqrt{(3/2)^2 + (1/2)^2} = \sqrt{5/2}$, and their in-plane spin angles are $\tan^{-1}(1/3)$, $\tan^{-1}(3)$, *etc*. Then the interactions of the four central sites with the next eight always involve the same absolute difference in in-plane angle, whose cosine is

$$\cos\left(\phi_1 - \phi_2\right) = \frac{\mathbf{r}_1 \cdot \mathbf{r}_2}{r_1 r_2} = \frac{\frac{1}{2}\cdot\frac{3}{2} + \frac{1}{2}\cdot\frac{1}{2}}{\frac{1}{\sqrt{2}}\cdot\frac{\sqrt{5}}{\sqrt{2}}} = \frac{2}{\sqrt{5}}. \tag{8.23}$$

There are a total of eight bonds connecting r_1-sites to r_2-sites, with their exchange energy being $8JS^2(1 - \frac{2}{\sqrt{5}}\sqrt{1 - m_1^2})$. The total energy in the first 12 bonds in the core region is then

$$E_{\text{core}} = -4JS^2\left(\lambda m_1^2 + \frac{4}{\sqrt{5}}\sqrt{1 - m_1^2} - 3\right). \tag{8.24}$$

The energies in bonds farther out from the core are ignored. One can see that for small m_1, there are two competing terms, and an expansion to quadratic order gives

$$E_{\text{core}} \approx -4JS^2\left[\frac{4}{\sqrt{5}} + \left(\lambda - \frac{2}{\sqrt{5}}\right)m_1^2 - 3\right]. \tag{8.25}$$

An in-plane vortex has all $m_j = 0$. This shows that the energy of an in-plane vortex will be reduced with non-zero m_1, provided that $\lambda > \frac{2}{\sqrt{5}}$. Therefore, the in-plane vortex will become unstable towards formation of an out-of-plane vortex at a critical anisotropy parameter $\lambda_c = \frac{2}{\sqrt{5}} \approx 0.894$, in this initial approximation.

The energy E_{core} in (8.24) can be analyzed more generally for arbitrary $m_1 < 1$ by finding the extrema, according to

$$\frac{\partial E_{\text{core}}}{\partial m_1} = -8JS^2 m_1\left[\lambda - \frac{2}{\sqrt{5}}\frac{1}{\sqrt{1 - m_1^2}}\right] = 0. \tag{8.26}$$

This has two solutions. The in-plane solution with $m_1 = 0$ exists for any λ, and has energy in these 12 bonds,

$$E_{\text{ip}} = 4JS^2\left(3 - 2\lambda_c\right), \quad \lambda_c = \frac{2}{\sqrt{5}}. \tag{8.27}$$

The out-of-plane solution exists only for $\lambda > \lambda_c$, with the out-of-plane component given by

$$m_1 = \sqrt{1 - (\lambda_c/\lambda)^2}\,. \tag{8.28}$$

This is zero at $\lambda = \lambda_c$ and then grows for $\lambda > \lambda_c$. The out-of-plane vortex energy in this approximation is

$$E_{\text{oop}} = 4JS^2\left(3 - \lambda - \lambda_c^2/\lambda\right), \quad \text{only for } \lambda > \lambda_c. \tag{8.29}$$

When the out-of-plane vortex is possible, E_{oop} is less than E_{ip}. Although both vortex types are possible for $\lambda > \lambda_c$, this explains why any small fluctuation will cause the in-plane structure to deform into an out-of-plane structure when $\lambda > \lambda_c$. This simple analysis shows that the energetics of the core region on a discrete lattice is responsible for the crossover from in-plane vortices for $\lambda < \lambda_c$ to out-of-plane vortices for $\lambda > \lambda_c$.

The calculation can be made more precise by considering sets of spins with non-zero m at larger radii. In addition to including four sites at radius $r_1 1/\sqrt{2}$ with $m_1 \neq 0$, the additional eight sites at radius $r_2 = \sqrt{5/2}$ with $m_2 \neq 0$ are included. These latter sites interact with another four sites (with $m_3 = 0$) at a third radius $r_3 = \sqrt{9/2}$. Including the total of 32 bonds among these 16 sites, the next approximation for the core exchange energy is

$$E_{core} = -4JS^2\left[\lambda\left(m_1^2 + m_2^2\right) + \frac{4}{\sqrt{5}}\sqrt{1 - m_1^2}\sqrt{1 - m_2^2} + \frac{4}{\sqrt{5}}\left(1 + \frac{4}{\sqrt{13}}\right)\sqrt{1 - m_2^2} + \frac{4}{5}\left(1 - m_2^2\right) - 8\right]. \tag{8.30}$$

The first term is the coupling of s^z-components; the remaining terms are the in-plane components. The variations with respect to m_1 or m_2 both are zero for an allowed solution:

$$\frac{\partial E_{core}}{\partial m_1} = -8\lambda(m_1 + m_2) + \frac{16}{\sqrt{5}}\frac{m_1}{\sqrt{1 - m_1^2}}\sqrt{1 - m_2^2} = 0 \tag{8.31a}$$

$$\frac{\partial E_{core}}{\partial m_2} = -8\lambda(m_1 + m_2) + \frac{16}{\sqrt{5}}\frac{m_2}{\sqrt{1 - m_2^2}}\left[\sqrt{1 - m_1^2} + \left(1 + \frac{4}{\sqrt{13}}\right)\right] + \frac{32}{5}m_2 = 0. \tag{8.31b}$$

It may not be easy to solve this nonlinear equation for m_1, m_2, but that is not necessary for determining the critical anisotropy. One only needs to assume that $m_1 = m_2 = 0$ for the in-plane vortex, and the value of λ at which they begin to take non-zero values is λ_c. This means an expansion of these equations for small values $m_1 \ll 1$, $m_2 \ll 1$, is all that is needed. That gives a pair of homogeneous linearized equations,

$$+(A - \lambda)m_1 - \lambda m_2 = 0 \tag{8.32a}$$

$$-\lambda m_1 + (B - \lambda)m_2 = 0 \tag{8.32b}$$

$$A = \frac{2}{\sqrt{5}}, \quad B = \frac{4}{\sqrt{5}}\left(1 + \frac{1}{\sqrt{5}} + \frac{2}{\sqrt{13}}\right). \tag{8.32c}$$

A non-trivial solution (the out-of-plane vortex) begins to appear only if the determinant D of the coefficients is zero:

$$D = (A - \lambda_c)(B - \lambda_c) - \lambda_c^2 = 0. \tag{8.33}$$

This gives the critical anisotropy parameter,

$$\lambda_c = \frac{AB}{A + B} \approx 0.716. \tag{8.34}$$

This is a considerable improvement over the initial approximation, and much closer to the value $\lambda_c \approx 0.72$ found in numerical simulations. Note that the *strength* of the easy-plane critical anisotropy is

$$\delta_c = 1 - \lambda_c \approx 0.284. \tag{8.35}$$

This procedure of discrete core analysis can be taken successively to larger core regions. By using three sets of sites with non-zero m_j, the critical parameter moves down to $\lambda_c \approx 0.7044$, somewhat smaller than the initial simulations on small systems. When simulations are performed for 50×50 or larger, one finds that indeed λ_c is actually slightly less than this value. Zaspel and Godinez [19] found a procedure to calculate the discrete vortex energy, successively summing over larger and larger core regions. A similar procedure can be applied to the calculation of the critical anisotropy, allowing for an extrapolation to the infinite sized limit [10], where $\delta_c \to 0.29659051$ ($\lambda_c = 0.70340949$). This result means than in any square-lattice materials where $\lambda < \lambda_c$, the static vortex structure is essentially planar, with no large out-of-plane component. This discrete analysis also is able to give the relative sizes of the m_j; it produces the profile of the out-of-plane vortex, at its stability limit. That is actually a dynamic mode of oscillation associated with the crossover between the two vortex types.

This same discrete core analysis can be extended to other lattices. For the triangular lattice (six nearest neighbors) one obtains $\delta_c \to 0.38714359$ ($\lambda_c = 0.61285641$), and for the hexagonal lattice (three nearest neighbors) one has $\delta_c \to 0.16704412$ ($\lambda_c = 0.83295588$). The greater concentration of sites in the triangular lattice makes the system more continuous, leading to a wider range of stability for the out-of-plane vortices. The opposite is true for the hexagonal lattice, which more greatly favors the in-plane vortices.

Overall, the results show that the vortex instability is a discrete lattice effect, something that cannot be described in the continuum limit. This is quite different from the instability found for kinks in a 1D easy-plane ferromagnet, using the continuum limit.

Exercise 8.3. Consider a vortex centered in a cell of a hexagonal lattice, surrounded by six nearest sites at distance $r_1 = 1$ with $s^z = m_1$, and another six second nearest sites at distance $r_2 = 2$ with $s^z = m_2$. Assume the in-plane structure given in (8.7), with a $q = 1$ vortex at the origin and $\phi_0 = 0$. (a) Show that the core energy in the 24 bonds among these sites is

$$E_{\text{core}} = -6JS^2\Big[\lambda\Big(m_1^2 + m_1 m_2\Big) + \frac{1}{2}\Big(1 - m_1^2\Big) + \sqrt{1 - m_1^2}\sqrt{1 - m_2^2} + \frac{5}{\sqrt{7}}\Big(1 - m_2^2\Big) - 4\Big] \tag{8.36}$$

(b) Defining a constant $A_{\text{h}} \equiv 1 + 5/\sqrt{7}$, show that the determinant of the resulting linearized stability system goes to zero at a critical anisotropy parameter given by

$$\lambda_c = -A_{\text{h}} + \sqrt{A_{\text{h}}(A_{\text{h}} + 2)} \approx 0.869. \tag{8.37}$$

Simulations find a vortex instability near $\lambda \approx 0.86$, see further discussion of vortex stability issues in [8–10].

8.4 Moving in-plane and out-of-plane vortices

Vortex motion couples the in-plane angle with the out-of-plane spin components, because ϕ_i and S_i^z are canonically conjugate coordinates. This means that even an in-plane vortex will develop non-zero out-of-plane spin components if it is moving at some velocity. Here we take a brief look at how vortex motion modifies the structures, and allows one to define vortex momentum and an effective mass. Taken together, these properties describe a magnetic vortex as a particle-like object, with an interesting dynamical equation of motion for its center.

The leading correction to vortex structure, due to motion at velocity $\mathbf{v}$, can be obtained from the dynamics equations (8.5) by assuming a traveling solution of the form $\mathbf{S}(\mathbf{r} - \mathbf{v}t)$, implying that the time derivative is replaced by $-\mathbf{v} \cdot \nabla$. At the same time, one can assume small perturbations ϕ_1 and m_1 on top of the static vortex solutions ϕ_0 and $m_0 = \sin\theta_0$ corresponding to the unperturbed vortex. The velocity $\mathbf{v}$ is also considered a small parameter of the same order as ϕ_1 and m_1. This is simple for the case of in-plane vortices, where initially $m_0 = \theta_0 = 0$. The dynamic equations linearized in the perturbations are now

$$-\mathbf{v} \cdot \nabla\phi_0 \approx JS\Big[\Big(4\delta - \big|\nabla\phi_0\big|^2\Big)\sin\theta_1 - (1 - \delta)\nabla^2\theta_1\Big] \tag{8.38a}$$

$$-\mathbf{v} \cdot \nabla\theta_1 \approx JS\ \nabla^2\phi_1. \tag{8.38b}$$

Away from the vortex center, we used $\nabla^2\phi_0 = 0$ from (8.11). It is difficult to obtain an exact solution even for this linearized system. That may not be too surprising,

considering that we know the continuum limit does not describe the vortex core correctly, which is exactly the region where all the interesting action is. Assuming δ might be close to unity, the first equation gives a result that has a singular point at $r = |q|/2\sqrt{\delta}$,

$$\sin\theta_1 \approx \frac{-\mathbf{v}\cdot\nabla\phi_0}{JS\left(4\delta - |\nabla\phi_0|^2\right)}. \tag{8.39}$$

Using (8.8), and $\hat{\boldsymbol{\varphi}} = \hat{\mathbf{z}} \times \hat{\mathbf{r}}$, this can be expressed as

$$\sin\theta_1 \approx \frac{q(\mathbf{v}\times\mathbf{r})\cdot\hat{\mathbf{z}}}{JS\left(4\delta\ r^2 - q^2\right)}. \tag{8.40}$$

This has been mostly applied to the simplest cases, $q = \pm 1$. Note that coordinate $\mathbf{r}$ is measured from the instantaneous location of the vortex core. Along a line through the vortex core and parallel to $\mathbf{v}$, one has $\theta_1 = 0$. Crossing this line, the sign of θ_1 reverses. This field then depends on the sine of the angle between $\mathbf{v}$ and $\mathbf{r}$. As a vortex moves through a square lattice, however, one can expect that the precise description of the vortex core is not contained in this solution. There will be strong discreteness effects if the core moves too close to a lattice site, violating the assumptions made to obtain the continuum limit.

By (8.38*b*), the perturbation ϕ_1 in the in-plane field is determined by θ_1, but one can see that the particular solution for ϕ_1 will be of the order of $\mathbf{v}^2$, hence, it is considered negligible to leading order.

For out-of-plane vortices, a similar perturbation analysis for a moving vortex can be performed [3]. However, the corrections θ_1 and ϕ_1 due to motion are both small compared to the original unperturbed angles. A very slight deviation in the out-of-plane structure similar to that for in-plane vortices appears, and in addition, the in-plane structure obtains a slight asymmetry on the line parallel to the velocity. The asymmetry that appears due to motion can be readily demonstrated by performing numerical simulations of a pair of vortices, for both in-plane and out-of-plane vortex types [4]. The radial dependence, however, may not follow expression (8.40) very closely in the core region: there is no sign change of θ_1 near $r = |q|/2\sqrt{\delta}$.

8.5 The vortex unbinding transition

Models with XY or easy-plane symmetry have always attracted much attention because of the presence of vortices and the existence of a special kind of phase transition, known as the BKT topological phase transition [11–13], associated with the thermal generation of vortices in VA pairs. Pair creation is also called *vortex unbinding*, imagining that before a pair is created, the vortex and anti-vortex are somehow coupled tightly together (this should not be taken literally, because they do not exist until they are created). Here we take a short look at some aspects of this transition, as obtained from combinations of MC and SD simulations.

According to the Ampere's law (8.10) for the gradient of the in-plane spin angle, the total vorticity within a boundary is quantized. If no vortices cross the boundary, the total vorticity is conserved, which implies that vortex charges can be created only

in VA pairs ($q = +1$ created along with $q = -1$). The pair interaction energy is shown later in (9.118) to depend on the separation of the vortex from the anti-vortex. This energy is in addition to self-energies for both the vortex and the anti-vortex, as given in (8.15). Although there is an energy cost for creation of a pair, it also increases the entropy of the system, which increases the likelihood of pair formation as the temperature is raised. We can obtain a very approximate estimate of the temperature at which VA pair formation becomes favorable, by asking what temperature is needed to make the change in free energy become negative.

A vortex could be created somewhere in a circular system of radius R, and its corresponding anti-vortex at another arbitrary location, separated by distance X_{12}. The two self-energies combined are approximately (at $\lambda = 0$, for in-plane vortices)

$$E_1 + E_2 = 2 \times \pi J S^2 \ln \frac{R}{r_0}, \tag{8.41}$$

where the short cutoff is on the order of $a/4$ in terms of the lattice spacing a (derived for square lattice). The pair interaction energy is

$$U_{\text{pair}} = 2\pi J S^2 q_1 q_2 \ln \frac{R}{X_{12}} = -2\pi J S^2 \ln \frac{R}{X_{12}}, \tag{8.42}$$

where the two vortices are of opposite sign. This is an attractive interaction that competes with the self-energies. The total energy change for creation of a pair is estimated as the sum,

$$\Delta E = E_1 + E_2 + U_{\text{pair}} = 2\pi J S^2 \ln \frac{X_{12}}{r_0}. \tag{8.43}$$

If the vortex and anti-vortex become free from each other, one can let $X_{12} \to R$, as the typical maximum separation. On the other side is the question of the entropy available for the pair creation, which is estimated very roughly by supposing that both the vortex and anti-vortex can be created almost anywhere in the system. Allowing the precision of a location to be on the order of r_0^2, the entropy change in the creation process is about

$$\Delta S \approx k_{\text{B}} \ln \left(\frac{R^2}{r_0^2} \times \frac{R^2}{r_0^2} \right) = 4 k_{\text{B}} \ln \frac{R}{r_0}. \tag{8.44}$$

Both the vortex and the anti-vortex contribute a factor within the logarithm. Then the change in Helmholtz free energy for a fixed temperature is estimated as

$$\Delta F = \Delta E - T \Delta S \approx 2\pi J S^2 \ln \frac{R}{r_0} - 4 k_{\text{B}} T \ln \frac{R}{r_0}. \tag{8.45}$$

The typical pair separation has been set to R. ΔF becomes negative at an estimate of the BKT unbinding temperature,

$$k_{\text{B}} T_{\text{c}} \approx \frac{\pi}{2} J S^2. \tag{8.46}$$

The particular number obtained here is not very precise, in fact, the number 0.699 replaces $\pi/2$ for the XY model ($\lambda = 0$). But the analysis shows that the entropy

available to vortex pairs is sufficient to overcome their energy cost, and once the temperature is high enough, thermally generated vortices and anti-vortices are a certainty. To obtain better estimates of T_c requires other theory or we can defer to MC simulations, which have the ability to find T_c as a function of anisotropy parameter λ and other factors.

8.6 Monte Carlo simulations of the Berezinskii–Kosterlitz–Thouless transition

A hybrid cluster MC method described in section 4.5.4 can be used to produce some thermal averages for the 2D XY model. Here we show some typical results that exhibit the main features of the BKT transition; this is a wide field of study and many other results can be found in the literature. Recall that the hybrid scheme described earlier involves a combination of single-spin Metropolis steps and over-relaxation steps that modify all spin components, and Wolff cluster steps acting only on the in-plane spin components. One MC step is the combination of an effective pass through the lattice by each of these methods. We show data using four to ten bins of 30 000 to 50 000 MCS for a total of 200 000 to 300 000 MCS. One can take averages over more bins and more MCS but for many quantities this is already sufficient to see the major trends. In addition, it is important to use a range of temperatures and system sizes; the variation with system size helps to determine T_c precisely according to finite size scaling methods. The calculations have been performed on $L \times L$ square lattice systems with periodic boundary conditions.

First consider the XY model ($\lambda = 0$). The internal energy per spin ($e = E/N = \langle H \rangle / N$) in figure 8.3 starts near zero at low temperature and has a slow rise with increasing T, but exhibits nothing dramatic. The specific heat per spin ($c = C/N$) also shown in figure 8.3 does show a strong peak whose position moves to lower temperature with increasing system size. However, c must tend to $c \to 1$ at $T \to 0$ (classical low-T limit for two degrees of freedom) and it also necessarily must tend to zero at very high T, because a spin system has a maximum energy state, unlike a usual mechanical system with a quadratic kinetic energy. For the largest systems the peak is near $k_B T/JS^2 \approx 0.73$.

The in-plane magnetic moment (m_{xy}, see figure 4.15) does make a dramatic drop to values close to zero, around the same region as the peak in specific heat. This quantity acts as an *order parameter* because it better indicates the geometrical structure in the average spin configuration. At low temperatures, neighboring spins are strongly correlated over a larger length scale known as the correlation length; the whole set of spins tend to move around together if the correlation length is of the order of the system size. Because we can only simulate a finite size, that limits the maximum correlation length and the drop of m_{xy} towards zero at T_c is rounded. In principle, m_{xy} would be zero for $T > T_c$ in an infinite sized system, but finite size effects prevent that.

The vortex unbinding can be seen by measuring the number density of vortices plus anti-vortices as a function of temperature. Vorticity can be found using a discrete version of Ampere's law (8.10) around each square cell or plaquette of the

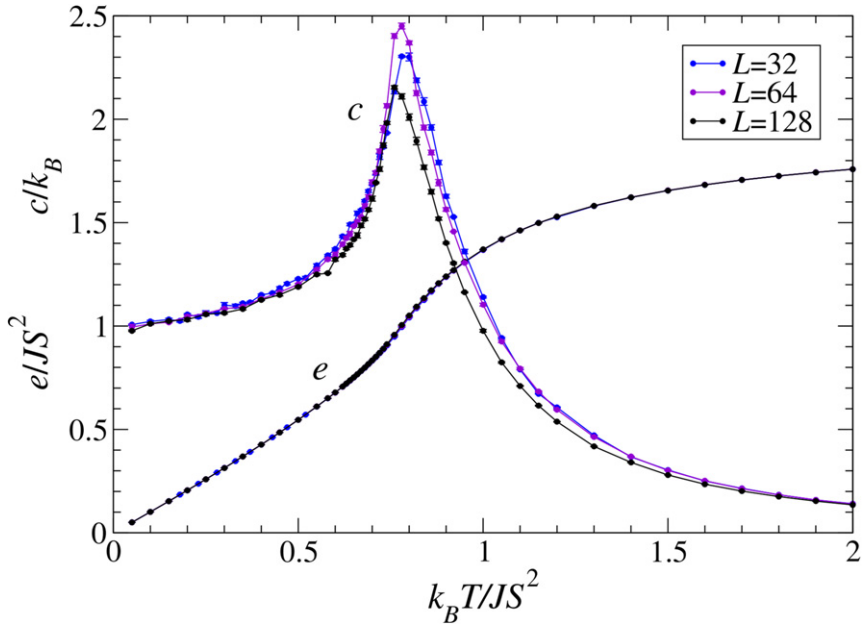

Figure 8.3. Energy and heat capacity per spin versus temperature in $L \times L$ XY models from the hybrid cluster MC simulations.

lattice. Each plaquette contains four spins and four bonds between neighboring spin pairs. Going in the counterclockwise sequence around a plaquette, one needs to form the sum of changes in in-plane spin angles, from which the vorticity within that path is found by

$$q = \frac{1}{2\pi} \sum_{\text{edge bonds}} \Delta\phi_{\text{bond}}. \tag{8.47}$$

The symbol $\Delta\phi_{\text{bond}}$ indicates the difference of two spin angles in a bond. $\phi_{i+1} - \phi_i$, taken in the counterclockwise sense and shifted into the branch $-\pi/2 \leqslant \Delta\phi_{\text{bond}} \leqslant +\pi/2$. This way, each plaquette has only the possible values $q = 0, \pm 1$. We should also like to mention that theoretically there is also the possibility of vortices with larger integral values, such as $q = \pm 2$. They can appear especially if there are vacancies or non-magnetic impurities in the lattice. A sum around the outside of a block of four neighboring plaquettes can be used to locate these higher vorticity charges. Then once all vortices of different charges are located, an averaged vortex number density ρ can be defined by dividing the total absolute charges by the number of sites,

$$\rho = \frac{1}{N} \sum_k |q_k|, \tag{8.48}$$

where k here labels the charges found. Note that if there are charges larger then ± 1 present they contribute with a weight proportional to the size of the charges. It is

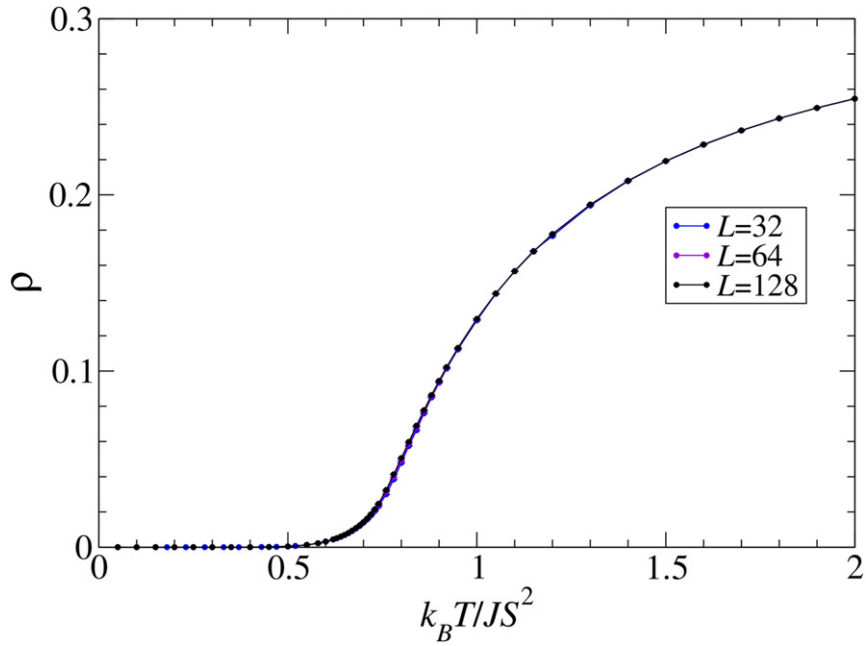

Figure 8.4. Number density of vortices (both charge signs) per unit cell versus temperature in $L \times L$ XY models from the hybrid cluster MC simulations.

possible to sketch a state where every plaquette has a unit charge, but alternating in signs. Then the maximum possible value is $\rho = 1$, however, that is an improbable higher energy state that will contribute little in thermal averages.

The resulting vortex number density $\rho(T)$ are shown in figure 8.4. The density is nearly zero for temperatures $k_BT/JS^2 < 0.5$, and starts to make a stronger rise around $0.6 < k_BT/JS^2 < 0.8$. There is very weak dependence on system size, with the initial rise in ρ occurring at slightly lower T for larger L. Ironically, the vortex density does not give a precise way to determine the critical temperature.

8.6.1 Estimations of the critical temperature—Binder's cumulant

A quantity that can sometimes indicate the precise location of T_c is Binder's fourth-order cumulant, denoted U_L. It is a quantity that indicates the shape of the probability distribution of the system magnetic moment, $\mathbf{M} = \sum_n \mathbf{S}_n$. Suppose a component M_x is being measured at high temperature. Because $\mathbf{M}$ is very random and typically of a small value, due to cancellations among the spins, one component M_x will tend to have a Gaussian distribution around a zero mean. On the other hand, at very low temperature, the whole system is in a highly correlated state, with all spins nearly parallel in the xy-plane (for models of easy-plane symmetry). The vector $\mathbf{M}$ will tend to be distributed mostly near a circle in the xy-plane of radius near NS. The corresponding distribution of a component M_x will not be Gaussian, but instead, have a minimum at $M_x = 0$ between two peaks at positive and negative values.

The moments of the spin distribution indicate its shape. Suppose one component M_x has a normalized Gaussian probability distribution for high temperature,

$$p(M_x) = \frac{1}{\sqrt{2\pi\sigma_x^2}} \exp\left\{-\frac{M_x^2}{2\sigma_x^2}\right\}. \tag{8.49}$$

The second- and fourth-order moments of this distribution are found by

$$\left\langle M_x^2 \right\rangle = \int_{-\infty}^{+\infty} \mathrm{d}x\ p(M_x) M_x^2 = \sigma_x^2 \tag{8.50a}$$

$$\left\langle M_x^4 \right\rangle = \int_{-\infty}^{+\infty} \mathrm{d}x\ p(M_x) M_x^4 = 3\sigma_x^4. \tag{8.50b}$$

Then for high temperature one has $\langle M_x^4 \rangle = 3\langle M_x^2 \rangle^2$. On the other hand, at very low temperature, with all spins nearly aligned, one expects $\langle M_x^4 \rangle = \langle M_x^2 \rangle^2$. For a single variable such as this, Binder's fourth-order cumulant is then defined by

$$U_L = 1 - \frac{\left\langle M_x^4 \right\rangle}{3\left\langle M_x^2 \right\rangle^2} \tag{8.51}$$

which takes the limiting values $U_L \approx 2/3$ at low temperature and $U_L \approx 0$ at high temperature, regardless of system size. Also at $T = T_c$ the spin distribution becomes independent of L and U_L is expected to have a universal value independent of L. Usually U_L is measured in a set of MC simulations with the curves for $U_L(T)$ at different L plotted together, and their common crossing point gives an estimate of T_c.

For the 2D XY model, the definition needs to be generalized to use both the x and y in-plane spin components. Each one will be Gaussian distributed with the same variance $\sigma_x = \sigma_y$ for high temperature. Then a sum $M_x^2 + M_y^2$ has the following leading order moments,

$$\left\langle M_x^2 + M_y^2 \right\rangle = \left\langle M_x^2 \right\rangle + \left\langle M_y^2 \right\rangle = \sigma_x^2 + \sigma_y^2 = 2\sigma_x^2 \tag{8.52a}$$

$$\left\langle \left(M_x^2 + M_y^2\right)^2 \right\rangle = \left\langle M_x^4 + 2M_x^2 M_y^2 + M_y^4 \right\rangle = 3\sigma_x^4 + 2\sigma_x^2\sigma_y^2 + 3\sigma_y^4 = 8\sigma_x^4. \tag{8.52b}$$

This shows that $\langle (M_x^2 + M_y^2)^2 \rangle = 2\langle M_x^2 + M_y^2 \rangle^2$ at high temperature, so it inspires the definition of the appropriate function for planar symmetry,

$$U_L = 1 - \frac{\left\langle \left(M_x^2 + M_y^2\right)^2 \right\rangle}{2\left\langle M_x^2 + M_y^2 \right\rangle^2}. \tag{8.53}$$

One sees that $U_L \approx 1/2$ at low temperature and $U_L \approx 0$ at high temperature, for any L. It is expected to have a universal value at T_c independent of L, as mentioned for the single component U_L, which is used to estimate T_c.

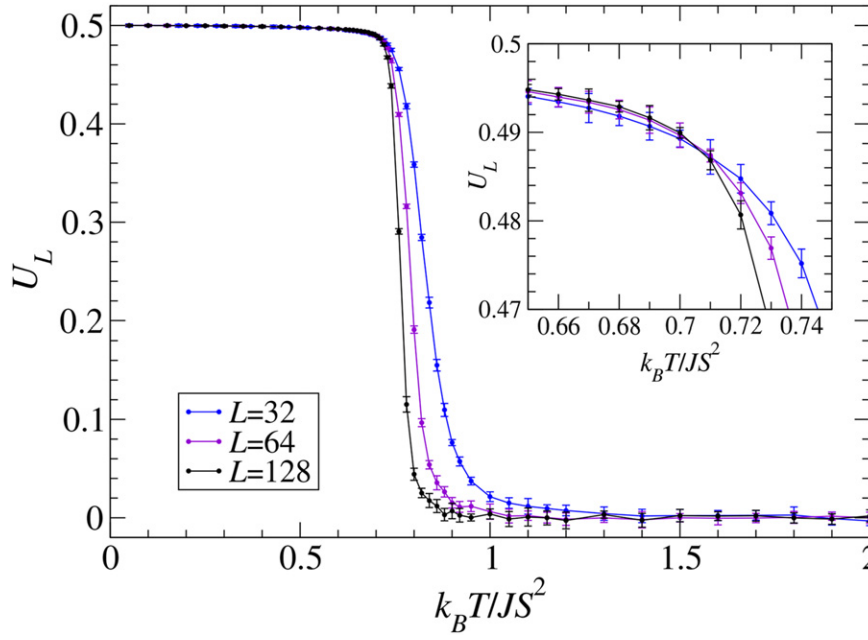

Figure 8.5. Binder's fourth-order cumulant as defined in (8.53) versus temperature in $L \times L$ XY models from the hybrid cluster MC simulations. The inset shows where the curves cross, which gives an estimate of the BKT transition temperature $k_B T_c/JS^2 \approx 0.70 - 0.71$.

A typical plot of U_L using definition (8.53) for different sizes is shown in figure 8.5. Although there is a crossing point, it is hard to locate unless the statistical noise in the data is very well under control. It does give an estimate of T_c for $\lambda = 0$ in the range $0.70 < k_B T_c/JS^2 < 0.71$. For the XY model the crossing appears too close to where $U_L \approx 1/2$, however, which means it is not the best way to find T_c.

Exercise 8.4. Check that the distribution $p(M_x)$ in (8.49) is correctly normalized, so that $\int_{-\infty}^{+\infty} \mathrm{d}x\, p(M_x) = 1$. Then verify the second- and fourth-order moments of the distribution in (8.50).

Exercise 8.5. Consider an isotropic Heisenberg model, with total magnetic moment $\mathbf{M} = (M_x, M_y, M_z)$. Show that an appropriate definition of the fourth-order cumulant that will distinguish the shape of the low and high temperature distributions of $\mathbf{M}$ is

$$U_L = 1 - \frac{3}{5}\frac{\langle \mathbf{M}^4 \rangle}{\langle \mathbf{M}^2 \rangle^2}. \tag{8.54}$$

What are the limiting values at low and high temperatures?

8.6.2 Estimations of the critical temperature—scaling of susceptibility

Binder's fourth-order cumulant can give an estimate of T_c for some models but it can require extensive calculations to obtain even two digit accuracy. A better approach has been to use the finite size scaling (FSS) of in-plane magnetic susceptibility χ_{xx}, such as that applied by Cuccoli *et al* [14] for $\lambda = 0$. In this theory, the in-plane susceptibility for temperatures near and below T_c is expected to follow a power law scaling with system size, according to the form

$$\chi_{xx} \propto L^{2-\eta}, \tag{8.55}$$

where $\eta(T)$ is the exponent for the in-plane spin–spin correlations below T_c. The exponent determines the large-distance form of decay of static spin–spin correlations. The static correlation function is $C^{xx}(\mathbf{r})$, as defined in (4.118). According to the BKT theory the spin–spin correlations are expected to be of power law form below T_c but change to a faster exponential form above T_c. To see this change in behavior, the correlation function has been plotted on a log-log scale in figure 8.6 for equally spaced temperatures from $k_B T/JS^2 = 0.1$ to $k_B T/JS^2 = 1.5$, for a 128×128 system. The expected behavior of the correlations is

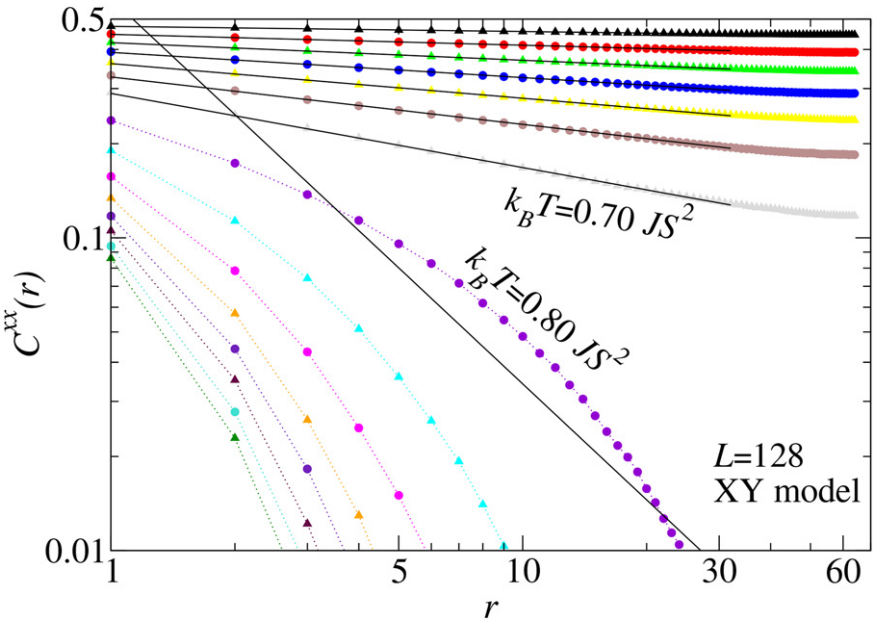

Figure 8.6. From hybrid cluster MC for 128×128 (data points), the static in-plane spin correlation function versus radius, for a sequence of evenly spaced temperatures $k_B T/JS^2 = 0.1, 0.2, \ldots 1.5$ (lowest T at top). Black lines are fits to power law decays $C^{xx} \propto r^{-\eta}$ using the data at $r \leqslant 32$, which works well only for $T < T_c$ where $k_B T_c/JS^2 \approx 0.70$. A fit is also shown for the data at $k_B T/JS^2 = 0.80$, which is poor because above T_c the correlations decay with an exponential form, see (8.56). Dotted lines on the higher temperature curves are guides for the eye, not fits.

$$C^{xx}(r) = \begin{cases} C_0 r^{-\eta} & T < T_c \\ C_1 r^{-1/2} \exp(-r/\xi) & T > T_c. \end{cases} \tag{8.56}$$

where C_0, C_1 are fitting constants and ξ is a *correlation length* in the state with unbound vortices, that also may depend on temperature. In figure 8.6 only fits to the power law form have been made, mostly for $T \leqslant T_c$, but also for one temperature above T_c. Only the data for $r \leqslant 32$ were used in the fits, because on a finite system, the correlation function is defined only to a maximum radius $L/2$, and we want to avoid the end region where finite size effects change the power law decay ($C^{xx}(r)$ must be symmetrical around $r = L/2$ in a finite system). The power law fits are very good for $T < T_c$. For $T < T_c$ the fits can be used to estimate $\eta(T)$, if desired, but a form that takes into account the limited system size is better. However, it is seen strikingly that the power law form does not work at all above the critical temperature.

Recalling the relation (4.120), it is then feasible that the exponent η appearing in the low temperature decay of $C^{xx}(\mathbf{r})$ should affect the scaling properties of χ_{xx} with system size. It is possible to take our MC results and fit χ_{xx} to the form (8.55) and extract $\eta(T)$ from the slope of $\ln(\chi_{xx})$ versus L, for each temperature simulated. However, the BKT theory determines that $\eta = 1/4$ at the critical point, regardless of the system size. Then, the FSS method to find T_c is to plot $\chi_{xx}/L^{2-\eta}$ versus temperature, for different system sizes. The resulting curves tend to cross at the universal point $\eta(T_c) = 1/4$, and even in XY systems with vacancies this crossing is a very sharp point. This type of plot is shown in figure 8.7. In order to display the details better, the error bars are not shown; the crossing is close to the point $k_B T_c/JS^2 \approx 0.700$, which is very good precision considering that the temperature increments of the MC simulation here were $k_B \Delta T/JS^2 = 0.01$ in these units. Then, for temperatures below T_c, the power law correlations of spin components, which are limited by the system size L, give one of the best ways to determine the transition temperature of the infinite sized system, T_c.

8.6.3 A measure of spin twist resistance—the helicity modulus

An easy-plane system also has another type of susceptibility, known as the helicity modulus per spin, $\Upsilon(T)$, that measures how the system reacts to imposing a slight spin twist Δ across the system along one coordinate. The helicity modulus maps over into superfluid density ρ_s according to $\Upsilon = (\hbar^2/m)\rho_s$, when the XY model is used to describe such a system with macroscopic quantum phase effects.

The spin twist would be an imposed angular displacement of the in-plane angle from one side of the system to the opposite side. It can be thought of as a generalized applied field, similar to a magnetic field. If the spins in the system are strongly correlated, as at low temperature, there will a strong resistance to a twist, and Υ is large. If the spins are more disordered and moving mostly independently, as at high temperature, there will be little resistance and Υ will be small. It can be expected that $\Upsilon(T)$ will diminish with temperature mostly in the region where vortices are being thermally produced, because the creation of VA pairs leads to weaker correlations for spins on opposite sides of the pairs.

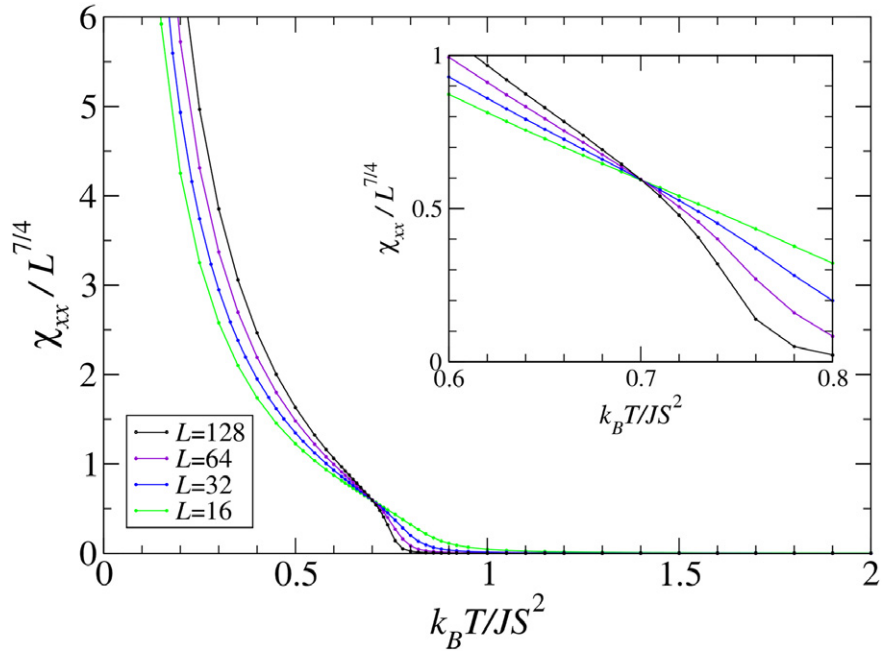

Figure 8.7. From hybrid cluster MC for the 2D XY model at different sizes $L \times L$, an in-plane susceptibility component (see the definition in (4.110)) scaled by $L^{2-\eta}$, under the assumption that $\eta(T_c) = 1/4$. The inset shows where the curves cross, which gives an estimate of the BKT transition temperature $k_B T_c/JS^2 \approx 0.70$. The error bars are suppressed to bring out the crossing point.

The definition of helicity modulus can be based on the free energy F, and finding the system's susceptibility to spin twists,

$$\Upsilon \equiv \frac{1}{N} \frac{\partial^2 F}{\partial \Delta^2}. \tag{8.57}$$

Compare the definition of magnetic susceptibility, equation (4.59). This definition is used in the limit of infinitesimal twist Δ. From the definition of free energy (4.34), the required derivative gives for any spin Hamiltonian,

$$\Upsilon = \frac{1}{N} \left\{ \left\langle \frac{\partial^2 H}{\partial \Delta^2} \right\rangle - \beta \left[\left\langle \left(\frac{\partial H}{\partial \Delta} \right)^2 \right\rangle - \left\langle \frac{\partial H}{\partial \Delta} \right\rangle^2 \right] \right\}, \tag{8.58}$$

where $\beta = (k_B T)^{-1}$. A simple model that imposes a twist on bonds in the $\hat{\mathbf{x}}$-direction is to modify the in-plane interactions in the spin Hamiltonian (8.2) into a form such as

$$\begin{aligned} J\left(S_i^x S_j^x + S_i^y S_j^y\right) &= JS^2 \sin\theta_i \sin\theta_j \cos\left(\phi_i - \phi_j\right) \\ &\longrightarrow JS^2 \sin\theta_i \sin\theta_j \cos\left(\phi_i - \phi_j - \Delta\right). \end{aligned} \tag{8.59}$$

The extra Δ inside the cosine then shifts the minimum angular displacement in the bond to Δ. In theory, it should only be included for bonds in one space direction. One then finds the following derivatives,

$$\frac{\partial H}{\partial \Delta} = J \sum_{(i,j)} \left(\hat{\mathbf{e}}_{ij} \cdot \hat{\mathbf{x}} \right) \left(S_i^x S_j^y - S_i^y S_j^x \right) \tag{8.60a}$$

$$\frac{\partial^2 H}{\partial \Delta^2} = \frac{1}{2} J \sum_{(i,j)} \left(S_i^x S_j^x + S_i^y S_j^y \right), \tag{8.60b}$$

where $\hat{\mathbf{e}}_{ij}$ is a unit vector in the direction from i to j, that selects only the bonds along one direction. Although $\frac{\partial H}{\partial \Delta}$ may have a small average value, its fluctuations contribute to Υ. The second partial derivative of H is seen to be half of the in-plane exchange energy. Once $\Delta \to 0$ is assumed, the direction of the bonds does not matter. Then these expressions can be implemented for MC calculations with symmetrization:

$$\frac{\partial H}{\partial \Delta} = \frac{1}{2} J \sum_{(i,j)} \left(S_i^x S_j^y - S_i^y S_j^x \right). \tag{8.61}$$

This averages over all nearest neighbor bonds. Note that each term is proportional to a triple cross product, $\hat{\mathbf{z}} \cdot (\mathbf{S}_i \times \mathbf{S}_j)$.

Exercise 8.6. Suppose a system has a spin twist field Δ that shifts the in-plane angles between neighboring spins along one direction, in a form such as that in (8.59), i.e. $\phi_i - \phi_j \to \phi_i - \phi_j - \Delta$. From the definition (4.34) of free energy F, verify that (8.58) for Υ results.

According to the renormalization group theory of Kosterlitz and Thouless [13], in an infinite system the helicity modulus jumps downward from a finite value $(2/\pi)k_B T_c$ at the critical temperature to zero for higher temperatures. This is similar in behavior to the average magnetic moment. Because the value at T_c is then known (but only for $L \to \infty$), this gives a way to estimate T_c, by plotting $\Upsilon(T)$ and marking its intersection with the straight line,

$$\Upsilon = \frac{2}{\pi} k_B T. \tag{8.62}$$

Examples of the application of this approach are given in figure 8.8(a) for the XY model and in figure 8.9(a) for the PR model. For the initial calculations of $\Upsilon(T)$, averages are from 3.2×10^5 to 1.28×10^6 MCS, with shorter runs on the larger systems for practical reasons. The curves of $\Upsilon(T)$ become steeper in the critical region as L increases. The intersection of the data with the straight line of (8.62)

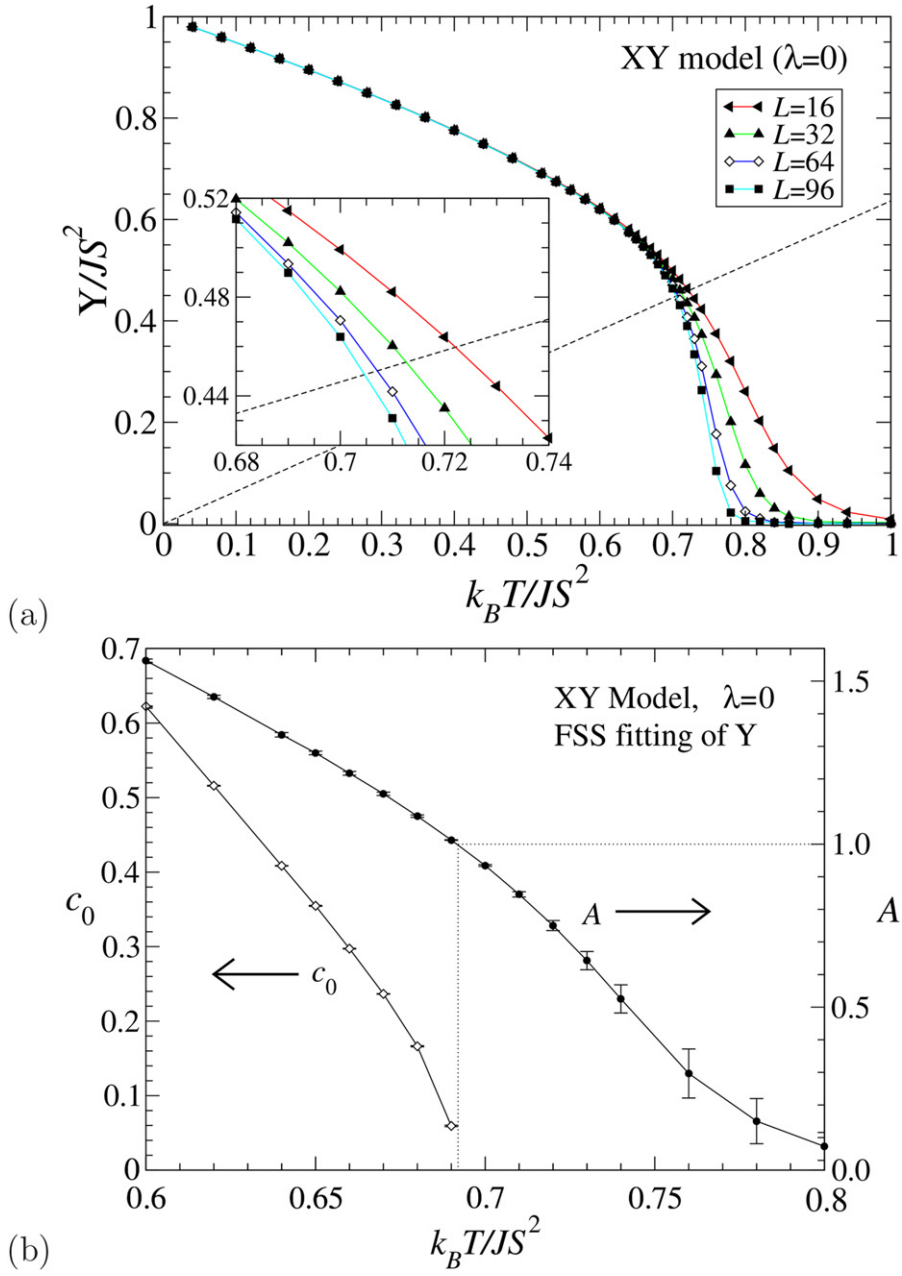

Figure 8.8. XY model ($\lambda = 0$) hybrid cluster MC results. (a) Helicity modulus $\Upsilon(T)$ as calculated using (8.58) on indicated $L \times L$ systems. The intersection of the dashed line (8.62) with the data gives an overestimate of the critical temperature, $k_B T_c/JS^2 \approx 0.705$. (b) FSS analysis of the same data by fitting to expression (8.63) for $T < T_c$ to obtain $c_0(T)$ and to expression (8.65) to obtain $A(T)$, leading to $k_B T_c/JS^2 \approx 0.692$ for the infinite system.

moves towards lower estimates of T_c for larger L. This method then always overestimates T_c, even at the largest possible L that can be simulated. At $L = 96$, it gives $k_B T_c/JS^2 \approx 0.705$ for the XY model and $k_B T_c/JS^2 \approx 0.912$ for the PR model. More data at $L = 160$ for the PR model change the estimate slightly, to $k_B T_c/JS^2 \approx 0.910$.

A finite size scaling analysis [15] can be used to improve the estimates. That theory shows that for temperatures below T_c, the helicity scales with system size according to [16]

$$\frac{\pi \Upsilon}{2k_B T} = 1 + c_0 \coth\left[2c_0 \ln(L/L_1)\right], \tag{8.63}$$

where c_0 and L_1 are fitting constants. This expression is valid only for $T < T_c$, and once the critical temperature is reached, the fitting constant c_0 goes to zero. The fits to MC with this expression also become very poor or nearly impossible once T passes above T_c. The fits are made versus different system sizes L, for a set of temperatures in the critical region. Note also that once $c_0(T)$ has been determined, then the estimate for the helicity modulus in the limit $L \to \infty$ is obtained as

$$\Upsilon_\infty(T) = \begin{cases} \dfrac{2}{\pi} k_B T[1 + c_0(T)] & T < T_c \\ 0 & T \geqslant T_c. \end{cases} \tag{8.64}$$

The helicity modulus jumps suddenly to zero at the transition.

Another scaling expression that has been widely applied for planar spin models is

$$\frac{\pi \Upsilon}{2k_B T} = A(T)\left[1 + \frac{1}{2\ln(L/L_0)}\right], \tag{8.65}$$

where both $A(T)$ and L_0 are fitting parameters. The expression is known to be exact at $T = T_c$, where $A(T_c) = 1$ also gives a method to obtain good estimates of the critical temperature. The expression does not fit very well for temperatures away from T_c, thus the appearance of a tight fit is a good indication of being close to T_c. Note that for the FSS approach to work well may require substantial computational effort, in order to have data with low enough statistical noise.

Examples of applying these scaling methods are shown in figure 8.8(b) for the XY model and figure 8.9(b) for the PR model. For the XY model, the same initial data used for systems with $L = 16$, 32, 64, 96 and 3.2×10^5 to 1.28×10^6 MCS were used to perform the scaling analysis. One finds that $c_0(L)$ can be fit quite well by expression (8.63), giving $c_0 > 0$, until T reaches 0.70, at which point a nonlinear least squares scheme (one found in the 'fit' command of gnuplot) is unable to come to convergence. The point where $c_0 \to 0$ should be T_c, but it is not exactly located. The fitting on $A(L)$ works both above and below T_c, and gives a value $A = 1$ at a temperature slightly higher than $k_B T/JS^2 = 0.69$. Thus, the two fittings bracket the

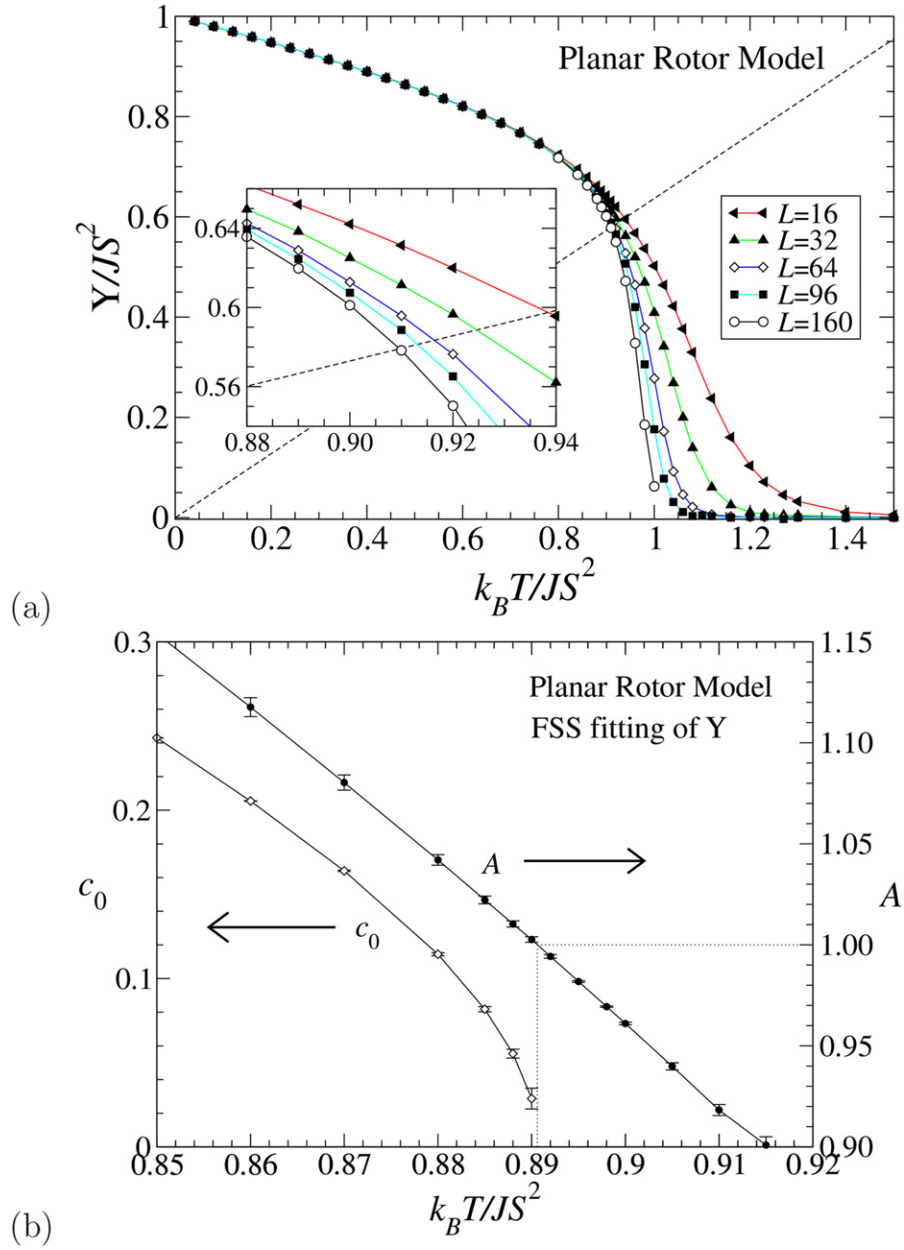

Figure 8.9. PR model (two-component spins) hybrid cluster MC results. (a) Helicity modulus $\Upsilon(T)$ as calculated using (8.58) on indicated $L \times L$ systems. The intersection of the dashed line (8.62) with the data gives an overestimate of the critical temperature, $k_B T_c/JS^2 \approx 0.912$. (b) FSS analysis of more extensive data at $L = 20, 32, 48, 64, 96$, fitting to expression (8.63) for $T < T_c$ to obtain $c_0(T)$ and to expression (8.65) to obtain $A(T)$, giving $k_B T_c/JS^2 \approx 0.891$ for the infinite system.

critical temperature, and combined they indicate $k_B T_c/JS^2 \approx 0.692$, slightly lower than that from using the susceptibility.

For the PR model, a new set of longer runs, all to 20×10^6 MCS, was made for temperatures near T_c, on systems with $L = 20, 32, 48, 64, 96$, to perform the FSS analysis. The result in figure 8.9(b) is quite consistent between where c_0 goes to zero and A goes to unity, leading to the estimate, $k_B T_c/JS^2 \approx 0.891$, rather high compared to the transition in the XY model. Of course, the extra S^z spin component present in the XY model is allowing the spins to move out of the xy-plane, causing their in-plane components to be shorter, on average. This implies a lower value of effective in-plane coupling JS_{xy}^2, hence the transition takes place at lower temperature in the XY model. One can come to the same conclusion by considerations of entropy for the two models.

One sees that the application of finite size scaling drastically improves the utility of the helicity data for estimations of T_c and extraction of the infinite sized limit.

8.6.4 Dependence of critical temperature on anisotropy and vacancies

It is interesting to consider the easy-plane model for different values of the anisotropy parameter λ, besides the case $\lambda = 0$ (the XY model). As λ is increased towards 1, the easy-plane anisotropy becomes weaker, and the spins can move more out of the xy-plane. This extra freedom of motion corresponds to greater out-of-plane fluctuations, and smaller typical in-plane spin components. The critical temperature for the XY model was found to be proportional to JS^2, however, one can think that S^2 in that expression is really the in-plane part of the spins, which now becomes smaller with weaker easy-plane anisotropy. This suggests that T_c should decrease as λ increases. This is indeed the case, as seen in the upper curve in figure 8.10, showing estimates of $T_c(\lambda)$ from finite sized scaling for model (8.2).

Another effect that has been of great interest, and which we only briefly touch on here, is the question of spin vacancies in the system. A small percentage of the lattice sites could be occupied by non-magnetic impurities, hence, those sites are not magnetically active and, for all practical purposes, behave as a missing site or spin vacancy. Although this might seem to be an unimportant perturbation to the system, even a few vacancies can have a drastic effect on both the static averages and the dynamics. In particular, simple calculations for individual vortices show that they will tend to be pinned on vacancies [17], which produce a strong pinning potential [18]. Furthermore, Zaspel *et al* [19] showed that a vortex formed around a vacancy will require weaker easy-plane anisotropy (smaller parameter δ) to remain in the in-plane state. While the critical anisotropy $\lambda_c \approx 0.7034$ for unpinned vortices, this changes to $\lambda_{cv} \approx 0.9545$ for a vortex pinned on a vacancy (both numbers for square lattice). The missing exchange bonds in the vicinity of the vacancy are responsible for the lower vortex energy there and the energetic preference to remain in the in-plane state with $s_z = 0$. Pereira and co-workers [20] also found that vacancies are responsible for causing oscillations of vortices and, in addition, an increasing density of vacancies further weakens their attractive potential [21] and the oscillation frequencies.

In the lower curve of figure 8.10, data are shown for $T_c(\lambda)$ with 16% of the sites randomly occupied by 'repulsive' vacancies [22], of density $\rho_{vac} = 0.16$, which were not allowed to be closer than the second nearest neighbor distance of $\sqrt{2}$. This model forces all vacancies to be surrounded with eight spin-occupied sites, which allows for each vacancy to be searched easily for the presence or absence of a pinned vorticity. In fact, this model produces pinned vorticities $q = \pm 2$ as well as the more usual $q = \pm 1$. One sees that in addition to the possibility of higher vorticity objects, the presence of vacancies lowers the BKT transition temperature. The maximum possible density of repulsive vacancies is $\rho_{vac} = 0.25$, however, because they are placed suddenly and randomly (or, *quenched*), the maximum density that can be placed is $\rho_{vac} \approx 0.1872$.

In another model of *randomly placed* vacancies [23], with no restrictions on their positions, their maximum density is not limited below unity. The hybrid cluster MC calculations on this model used averages over 4 to 64 realizations of the vacancy positions, on $L \times L$ systems with $L = 16$, 32, 64, 96 and 160. T_c could be found most precisely by fitting $C^{xx}(r)$ to power law form and locating the point where $\eta(T) = 1/4$. The results were also verified by comparison with Binder's fourth-order cumulant and the helicity modulus. For instance, figure 8.11 shows the trends in $\Upsilon(T)$ with increasing vacancy density. The intersection of the data with the straight line of (8.62) monotonically moves to lower T with increasing ρ_{vac}, exhibiting a striking trend. When many vacancies are present, the lattice becomes

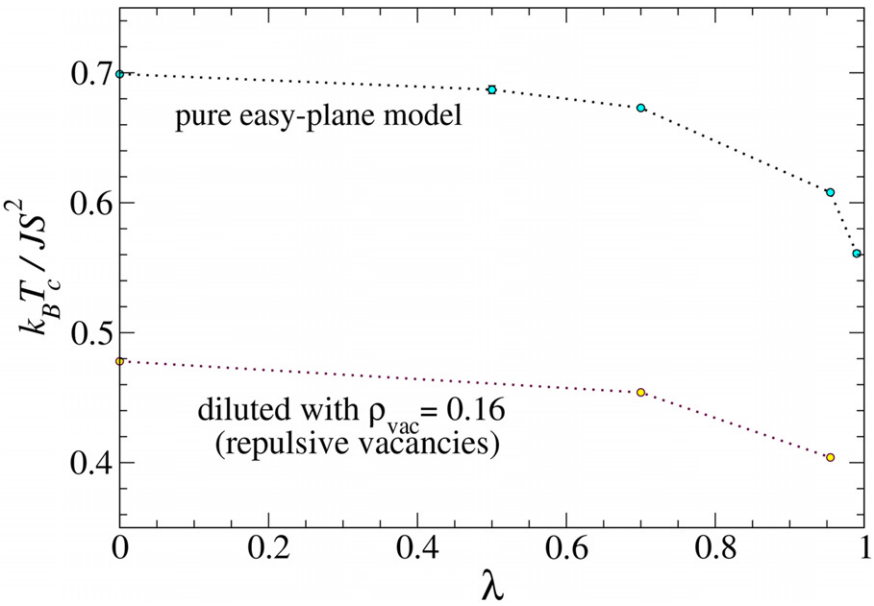

Figure 8.10. From scaling analysis of susceptibility and also checked by Binder's fourth-order cumulant, results for the BKT transition temperature in the easy-plane model (8.2) from hybrid cluster MC. The upper curve is the square lattice model, fully occupied, while the lower curve is a square lattice model with 16% of the sites occupied by repulsive vacancies. Dotted lines are guides for the eye.

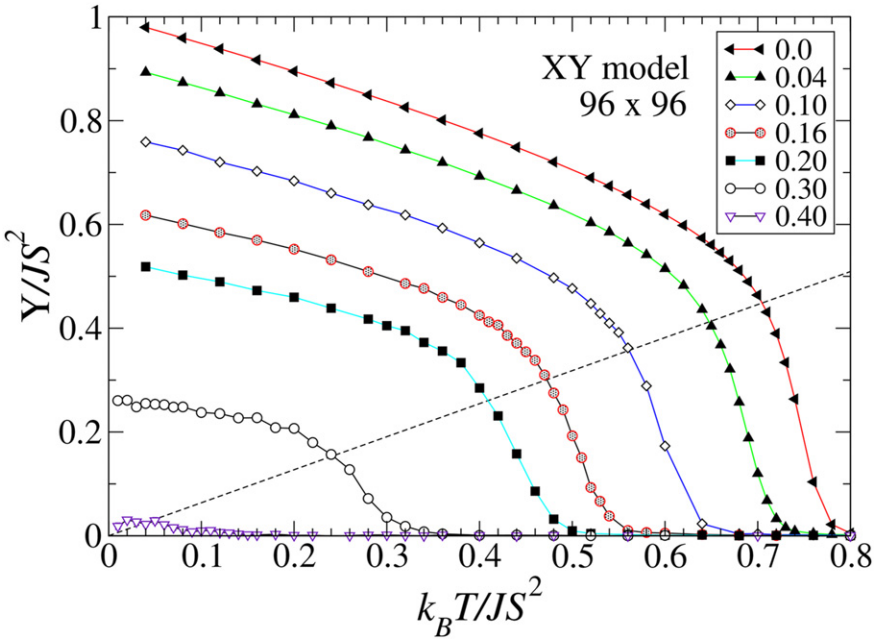

Figure 8.11. Results for helicity modulus versus temperature in the square lattice XY model with random vacancies, as calculated from expression (8.58) in hybrid cluster MC. Curves are labeled by the vacancy density ρ_{vac}. The dashed line is (8.62), whose intersection with the data gives an estimate of T_{c}. No transition is present for $\rho_{\text{vac}} > 0.41$, which coincides with the percolation limit.

rather disconnected, and this causes greatly weakened exchange interactions and correlations. This results in a lowering of T_{c} with increasing vacancy density, see figure 8.12. The effect of lower T_{c} with increasing ρ_{vac} is so strong that around a vacancy density of $\rho_{\text{vac}} \approx 0.41$, the transition temperature goes to zero. This vacancy density is then seen to be complementary to the site percolation threshold of about $p_{\text{c}} \approx 0.59$ for a square lattice, which is the minimum site density needed to have a connection across the system. Thus, the BKT transition is only present as long as the lattice is sufficiently occupied that the exchange interactions are able to percolate throughout the entire system. There must be sufficient couplings to lead to a correlation length equal to the system size at $T = T_{\text{c}}$. Note that even though the system may be somewhat disconnected due to all the vacancies, even so, at the critical temperature all spins in the system tend to be strongly correlated, which means that a cluster update scheme is still a necessity for accurate results. See [23] for further details.

Exercise 8.7. Consider a square lattice with a vacancy (missing spin) at the origin. Assume that a nearly planar vortex with in-plane angles from (8.7) is centered on the missing site. (a) Using the nearest out-of-plane spin components m_1 at radius $r_1 = 1$ (four sites) and m_2 at radius $r_2 = \sqrt{2}$ (four sites), estimate the core energy $E_{\text{core}}(m_1, m_2)$ for a vortex pinned on the vacancy. (b) Perform the

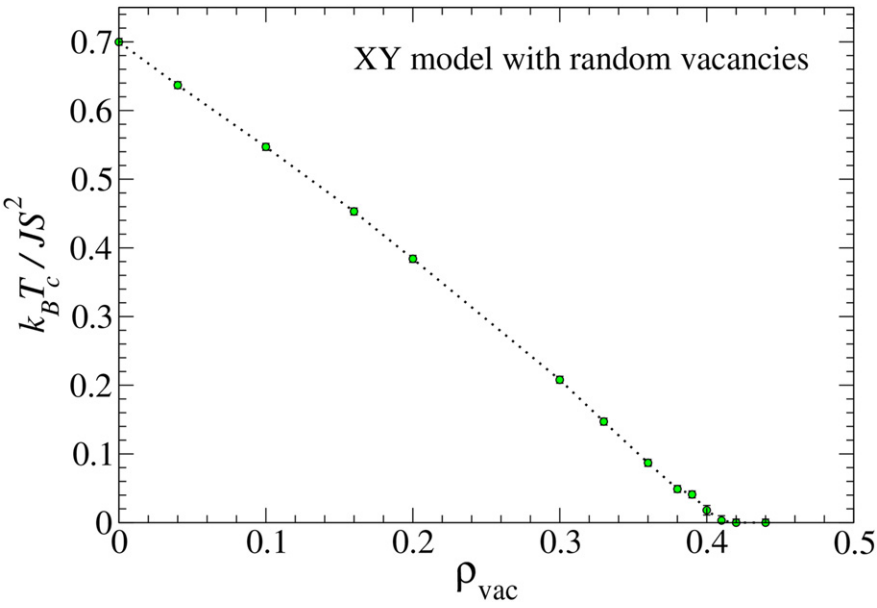

Figure 8.12. From scaling analysis of susceptibility and also checked by helicity modulus [23], results for the BKT transition temperature in the square lattice XY model (8.2) with $\lambda = 0$ from hybrid cluster MC, with randomly placed vacancies of density ρ_{vac}. The dotted line is a guide for the eye.

stability analysis in the limit $m_1 \ll 1$ and $m_2 \ll 1$, and estimate the critical anisotropy parameter λ_{cv} where the planar pinned vortex develops non-zero out-of-plane components.

8.7 Dynamic correlations in XY models

So far, we have discussed mostly the static properties due to vortices in thermal equilibrium in easy-plane models. Now we consider some aspects of the time-dependent response, especially, in the space- and time-dependent *dynamic correlation functions* or dynamic structure functions, such as $S^{xx}(\mathbf{q}, \omega)$. The basic definition and properties of $S^{xx}(\mathbf{q}, \omega)$ were introduced in section 5.7.5. The dynamic structure function gives an indication of the types of excitations in the system, in terms of indicating what frequency oscillations are present at a chosen wave vector $\mathbf{q}$. A significant intensity in $S^{xx}(\mathbf{q}, \omega)$ usually gives a direct indication of the spin wave spectrum, which appears as sharp peaks for $\mathbf{q}$ and ω related by the spin wave dispersion relation. For more localized objects such as vortices, the space Fourier transform (FT) of such a structure determines its intensity in $\mathbf{q}$-space, and its motion if present determines how intensity in $S^{xx}(\mathbf{q}, \omega)$ appears as a function of frequency.

The dynamic correlation function is the space–time FT of a space and time displaced spin pair correlation function. The definition (4.118) for the static correlations $C^{xx}(\mathbf{r})$ was generalized in (5.189) to include time displacement. We

apply it here in discrete form using **n** to represent lattice sites and **r** the possible displacements, using unit spins,

$$C^{xx}(\mathbf{r},\, t) = \frac{1}{N}\sum_{\mathbf{n}}\frac{1}{N_t}\sum_{t_0}\left\langle s^x_{\mathbf{n}}(t_0)s^x_{\mathbf{n}+\mathbf{r}}(t_0+t)\right\rangle \tag{8.66}$$

N is the total number of spin sites and N_t is the number of time samples. This function averages pairs of spins at constant space and time displacements **r** and t, respectively. The sums can be changed to integrations if a continuum expression is needed. We are not subtracting out the thermal average values, as was introduced originally for the static correlations, equation (4.118). The dynamic correlation function is the space and time FT, but converted to continuum weight as explained in chapter 5 in the derivation of (5.195). The structure functions are defined per frequency per squared wave vector, so the fundamental physical unit is $(JS)^{-1}a^2$.

We can calculate $S^{xx}(\mathbf{q},\, \omega)$ from data on a discrete space–time grid from simulations. The most efficient way to achieve this is via the convolution theorem and using the relation (5.205). For convenience we change to a dimensionless quantity, taking out the units,

$$S^{xx}(\mathbf{q},\, \omega) = \left(\frac{JS}{a^2}\right)\times\left(\frac{2\pi}{t_{\text{end}}}\frac{2\pi}{N_x a}\frac{2\pi}{N_y a}\right)\left\langle |A^x(\mathbf{q},\, \omega)|^2\right\rangle. \tag{8.67}$$

This is determined from the space–time FT of the unit spin field,

$$A^x(\mathbf{q},\, \omega) = \left(\frac{t_{\text{end}}}{2\pi N_t}\right)\sum_{t_l}\left[\left(\frac{a}{2\pi}\right)^2\sum_{\mathbf{r}} s^x_{\mathbf{r}}(t_l)\mathrm{e}^{-\mathrm{i}\mathbf{q}\cdot\mathbf{r}}\right]\mathrm{e}^{\mathrm{i}\omega t_l}. \tag{8.68}$$

Recall from chapter 5 that these are applied to a $N_x \times N_y$ system that is integrated over time out to final time t_{end} using a sequence of N_t time steps, and **q** and ω are discrete variables in a simulation. Obviously the correlations of other spin components, $S^{yy}(\mathbf{q},\, \omega)$ and $S^{zz}(\mathbf{q},\, \omega)$ can be defined as well. For XY symmetry models, one should have $S^{xx}(\mathbf{q},\, \omega) = S^{yy}(\mathbf{q},\, \omega)$. In simulations, we calculate both S^{xx} and S^{yy} separately and then average them together into one in-plane structure function.

8.7.1 Hybrid Monte Carlo–spin dynamics simulations

The hybrid MC–SD approach for the thermal time dynamics of spin systems was introduced in section 5.3. Here we describe a few details of that approach and discuss the main results, especially concerning the dynamic correlations.

The data shown here have been produced for a 128×128 system. The initial part of the calculation is the hybrid cluster MC method that combines Wolff cluster moves with over-relaxation and Metropolis single-spin steps. For a given temperature, the system was first equilibrated for $N_{\text{skip}} = 20\,000$ MCS. Then, a total of 500 000 MCS were made, saving a configuration of the system every 1000 MCS.

That produces $N_s = 500$ different states that were used to initiate the time integration. N_s is also the number of states from the ensemble that are used for averages.

For the time integration, the system was integrated using RK4 with an algorithm time step $\Delta t_a = 0.04(JS)^{-1}$, which is adequate for good energy conservation. Note that the Landau–Lifshitz equations of motion are integrated *without damping*, such that the motion takes place in the microcanonical ensemble. However, the results from the N_s different initial conditions will be averaged over in the canonical ensemble for the chosen temperature of the MC. The algorithmic time step Δt_a is rather short. Therefore, data for finding time FTs were saved at the data time interval $\Delta t = 6\Delta t_a$, which allows for the investigation of lower frequency responses. In order to take advantage of a fast FT (FFT) algorithm, the total number of data points in time should be a power of 2, for the most commonly used algorithms. Therefore we used total time samples $N_t = 2^p$, with FFT index $p = 12$ producing 4096 time samples. Thus, the interval of time integration for one initial condition is

$$t_{\text{end}} = N_t \Delta t = 2^{12} \times 6 \times 0.04(JS)^{-1} = 983.04(JS)^{-1}. \tag{8.69}$$

This implies that the lowest non-zero frequency to be analyzed in the FFT is

$$\Delta\omega = \omega_1 = \frac{2\pi}{t_{\text{end}}} = 6.3916 \times 10^{-3}(JS). \tag{8.70}$$

The resulting FTs have 4096 frequency points, however, because periodicity in time is imposed, the second half of the FT is symmetric with the first half, and contains no extra information (aliasing). For this reason, only about the first quarter of the final FFT data are useful. We avoid the part affected by aliasing and we focus on the low frequency part of the spectrum.

For the FT in space, a lattice of 128×128 has a very large number of possible wave vectors. There is no practical need to have data for every possible $\mathbf{q}$, instead, it is already very useful to produce only the space FT data at selected $\mathbf{q}$. We used only $\mathbf{q} = (q_x, 0)$, $(0, q_x)$ and (q_x, q_x), for $q_x = 2\pi m/L$, $m = 0, 1, 2 \ldots L/2$. The limited values of $\mathbf{q}$ mean that an FFT is not needed, rather, the space FT is performed with the help of a table of the appropriate needed phase factors $\exp(i\mathbf{q} \cdot \mathbf{r})$, which are constant during the calculations.

8.7.2 Low temperature dynamic structure function

At low temperatures $T < T_c$ the primary excitations present are spin waves. This is seen easily in the dynamic structure functions, some examples of which are shown in figure 8.13 for $k_B T = 0.1JS^2$. Note that S^{xx} is has been calculated as the average of xx and yy spin component correlations, due to the XY symmetry. Wave vectors of the form $\mathbf{q} = (q_x, 0)$ with $q_x = 2\pi m/L$ and m incremented by 4 are displayed. Essentially the only feature present in S^{xx} and also in S^{zz} is a very narrow peak, at the same location in both S^{xx} and S^{zz}, whose position shifts with $\mathbf{q}$. At low wave

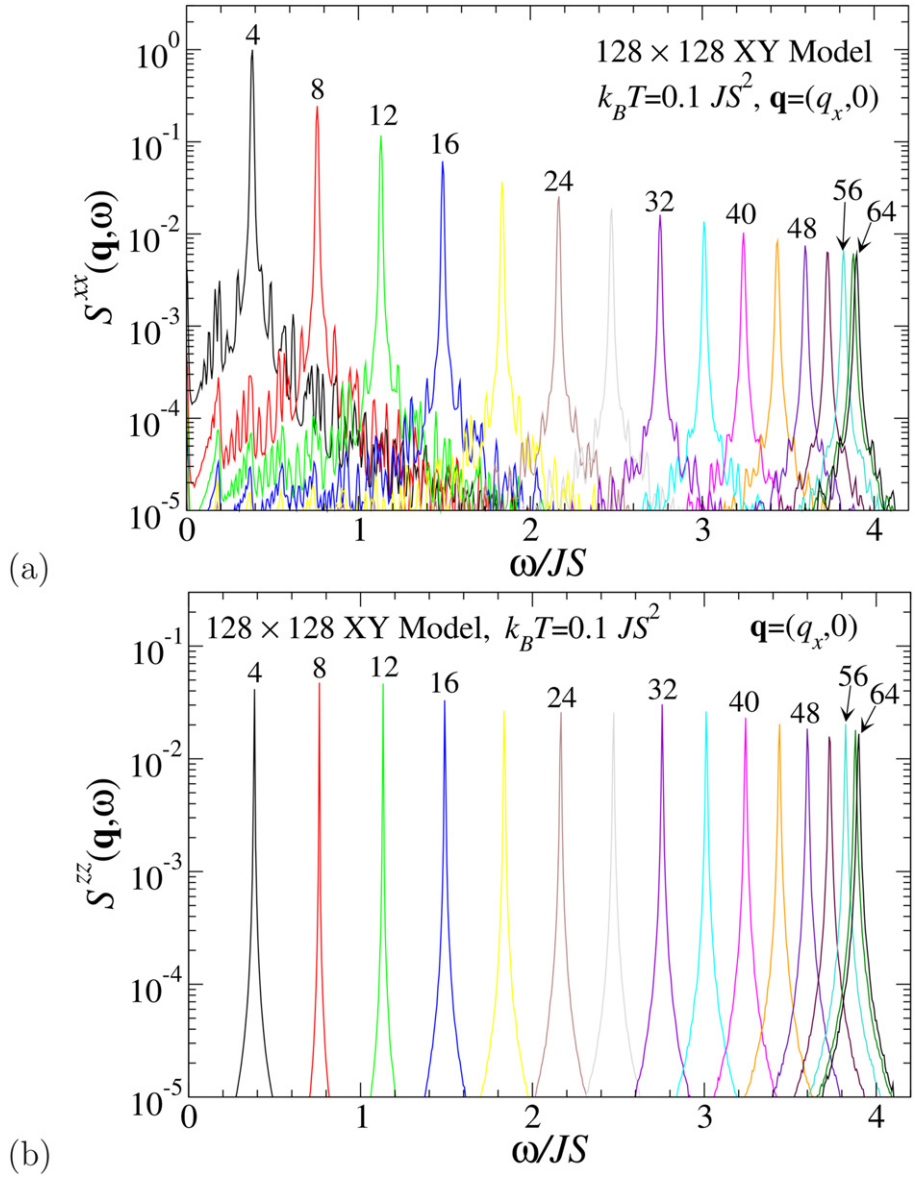

Figure 8.13. Dynamic structure functions (a) in-plane, $S^{xx}(\mathbf{q}, \omega)$ and (b) out-of-plane, $S^{zz}(\mathbf{q}, \omega)$, for the square lattice FM XY model ($L = 128$, $\lambda = 0$) at $k_B T = 0.1JS^2$, obtained from hybrid cluster MC combined with SD, from averages over 500 initial states, as explained in the text. The wave vectors are $q_x = (2\pi/L)m$ with index m in increments of 4, as indicated.

vectors the in-plane intensity is stronger; at the highest wave vectors, the out-of-plane intensity is more dominant. The peak location is then used to map out the dispersion relation for spin waves, $\omega(\mathbf{q})$, and the simulations give its temperature-dependence. One should also mention that there are many smaller subpeaks present

in $S^{xx}(\mathbf{q}, \omega)$; especially for smaller $\mathbf{q}$. These can be attributed to finite size effects and spin wave interference effects [24], that depend on the system size L. For the most part, compared to the spin wave peak the subpeaks are weak and become smeared out with increasing temperature.

Another example of the behavior of the structure functions is given in figure 8.14, at a slightly higher temperature, $k_B T = 0.4JS^2$, still below the transition temperature $k_B T_c \approx 0.70JS^2$. Now, the peaks for any chosen $\mathbf{q}$ have shifted to slightly lower frequency and their widths have increased due to the greater thermal fluctuations. Even so, the spin wave peak is the only significant feature in the structure functions.

A third example is given in figure 8.15 for a temperature approximately the same as the critical temperature, $k_B T = 0.7JS^2$. Now, the behavior of the curves is significantly different, with the growth of much stronger intensity appearing in the low frequency range, below the spin wave peak, primarily for $S^{xx}(\mathbf{q}, \omega)$. This is referred to as a *central peak* (CP). At this temperature, it is relatively weak, compared to the height of the spin wave peak. The in-plane response has the appearance of a spin wave peak riding on top of a wider background. The out-of-plane response has more the appearance of significantly broadened spin waves.

The spin wave dispersion relation $\omega(\mathbf{q})$ for the 2D XY ferromagnet on a square lattice, obtained by MC–SD, can be obtained from the peaks in the structure function $S^{xx}(\mathbf{q}, \omega)$, for a range of $\mathbf{q}$. The results in figure 8.16 have been displayed for the three temperatures below or near T_c, at wave vectors along both the (10)-direction and the diagonal (11)-direction. The solid curves are the $T = 0$ linearized spin wave theory, equation (6.36). The obvious feature of the simulation data is that the spin wave frequency for finite temperature becomes less than the linearized theory predicts. This spin wave *softening* is a typical effect due to thermal fluctuations, which weaken the effective or thermally averaged nearest neighbor exchange interactions, and hence the frequencies. One way to describe this effect theoretically is an approach known as the self-consistent harmonic approximation, which involves a temperature-dependent rescaling of J. Furthermore, the spin wave peak cannot be easily identified for $T > T_c$, especially at small wave vectors, because it becomes lost in the CP of $S^{xx}(\mathbf{q}, \omega)$. This is a rather dramatic effect and again it is closely associated with the BKT transition.

8.7.3 Higher temperature dynamic structure function and central peak

A fourth example of the dynamic structure functions is given in figure 8.17, for a temperature above the critical temperature, $k_B T = 0.9JS^2$. In this case, the response in $S^{xx}(\mathbf{q}, \omega)$ at the lower wave vectors has lost the spin wave peak. The only significant feature is a fairly wide CP. At the larger wave vectors closer to the edge of the Brillouin zone, there is a weak signature of the spin wave. In the out-of-plane correlations of $S^{zz}(\mathbf{q}, \omega)$, the spin wave peak can be identified for all the wave vectors. The curves there have the appearance of a spin wave signature riding on top of a broader but weak CP. Also, at these higher temperatures, the tails are fairly smooth and do not exhibit any features due to finite size effects.

The appearance of the CP as the temperature passes T_c can be illustrated further by replotting some results at particular $\mathbf{q}$'s on a linear scale, for the sequence of

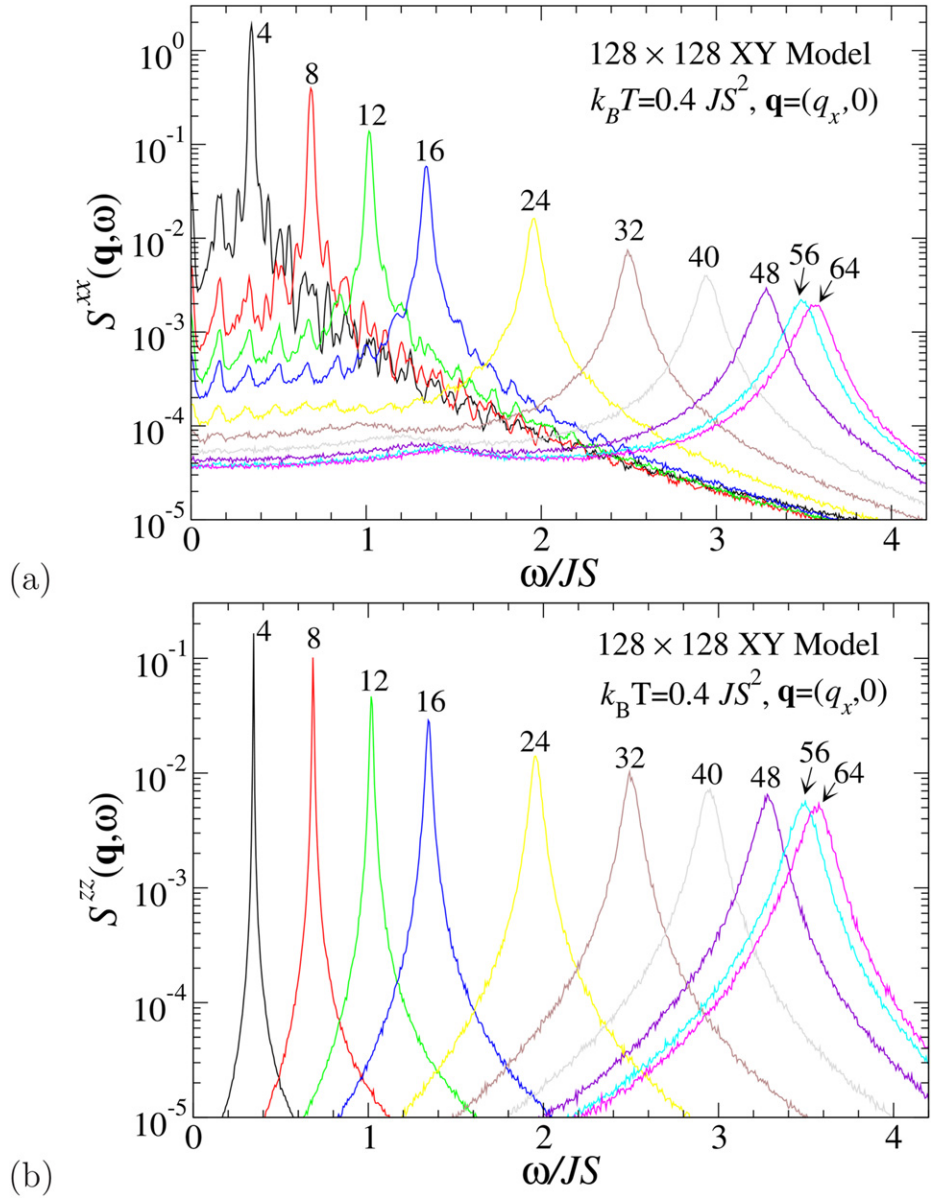

Figure 8.14. Dynamic structure functions (a) in-plane, $S^{xx}(\mathbf{q}, \omega)$ and (b) out-of-plane, $S^{zz}(\mathbf{q}, \omega)$, for the square lattice FM XY model ($L = 128$, $\lambda = 0$) at $k_B T = 0.4JS^2$, from averages over 500 initial conditions, with each $q_x = 2\pi m/L$ for indicated m values. Note the shifts of the peaks to lower frequencies and their increased widths compared to $k_B T = 0.1JS^2$ in figure 8.13.

temperatures. The first example is seen in figure 8.18 for the wave vector index $m = 8$ which gives $\mathbf{q} = (\pi/8, 0)$. The curves are labeled by dimensionless temperature variable $\tilde{T}$, defined from

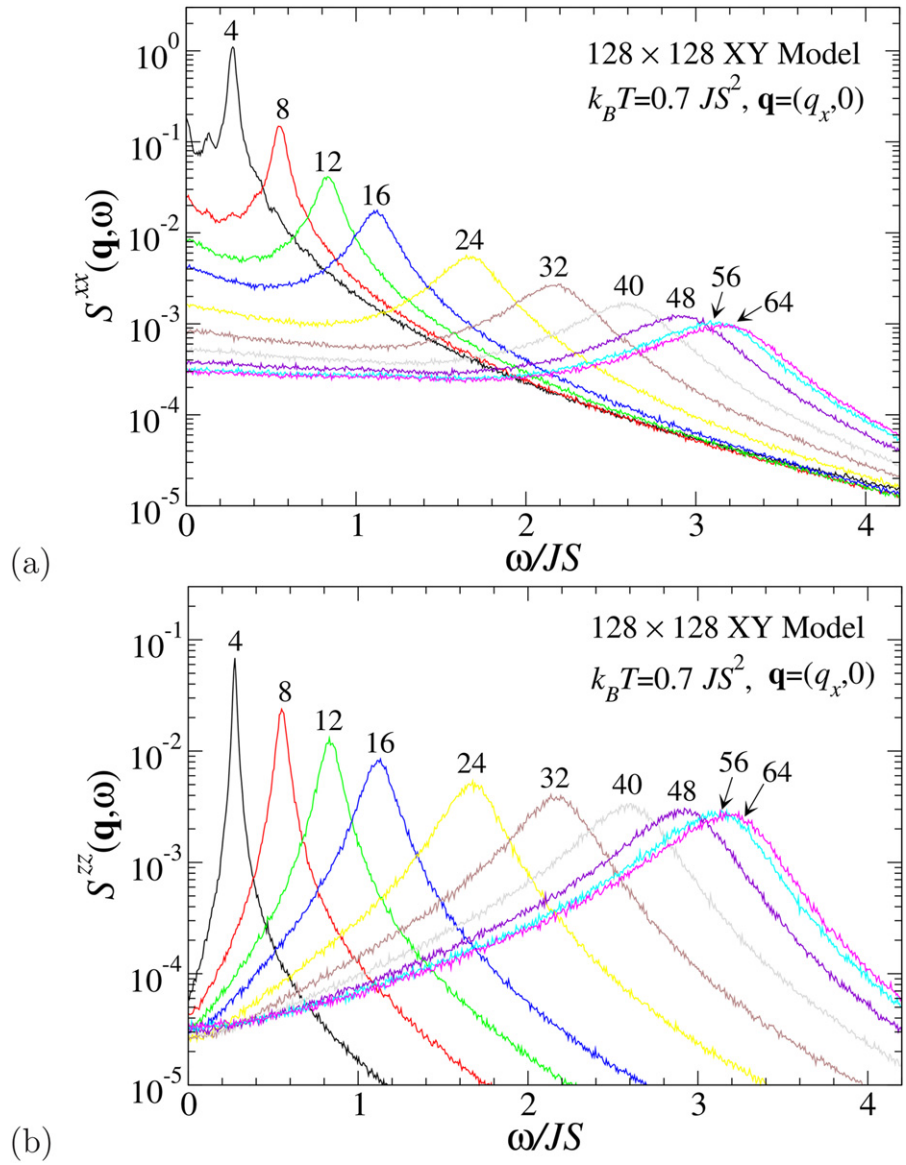

Figure 8.15. Dynamic structure functions (a) in-plane, $S^{xx}(\mathbf{q}, \omega)$ and (b) out-of-plane, $S^{zz}(\mathbf{q}, \omega)$, for the square lattice FM XY model ($L = 128$, $\lambda = 0$) at $k_B T = 0.7JS^2$, from averages over 500 initial conditions, with each $q_x = 2\pi m/L$ for indicated m values. Note the presence of CP intensity primarily in S^{xx}.

$$\tilde{T} \equiv k_B T/JS^2. \tag{8.71}$$

For $S^{xx}(\mathbf{q}, \omega)$, the relatively sharp spin wave peaks at $\tilde{T} < 0.7$ have minimal intensity in the low frequency region. For $\tilde{T} = 0.7 \approx \tilde{T}_c$, there is a weak low frequency tail of the spin wave that extends to $\omega = 0$. At the higher temperature $\tilde{T} = 0.9$, $S^{xx}(\mathbf{q}, \omega)$ does not exhibit any spin wave peak, but only CP intensity.

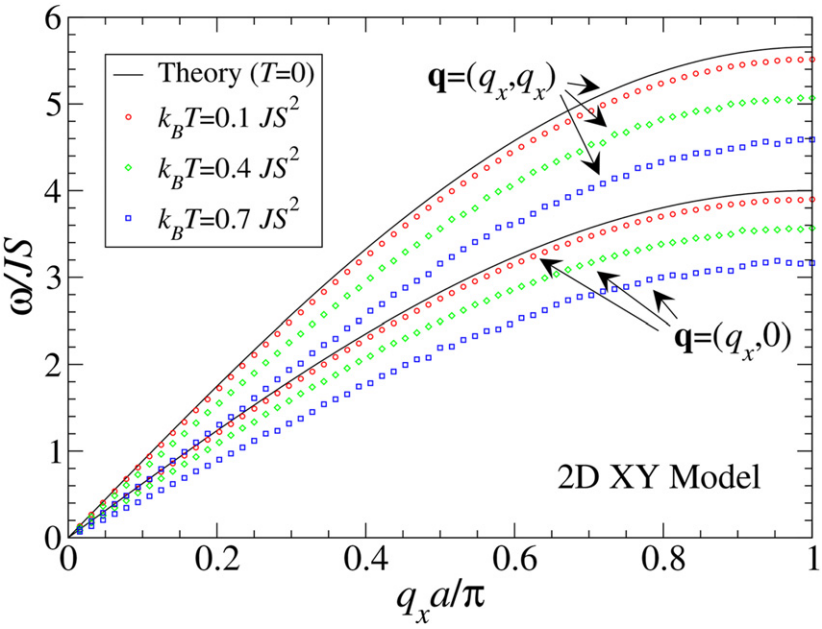

Figure 8.16. The spin wave dispersion relations $\omega(\mathbf{q})$ for the square lattice FM XY model (8.2) with $\lambda = 0$ obtained from hybrid cluster MC combined with SD, using the peak found in $S^{xx}(\mathbf{q}, \omega)$. Solid curves are the $T = 0$ spin wave theory, equation (6.36). The spin wave frequencies at the indicated $T > 0$ were obtained from the peak in $S^{xx}(\mathbf{q}, \omega)$ for wave vectors along both (10)- and (11)-directions. At $k_B T > 0.7JS^2$ the spin wave peak is not distinct from the CP, so $\omega(\mathbf{q})$ was not be estimated.

The spin wave does appear as a reasonably strong but wide peak in $S^{zz}(\mathbf{q}, \omega)$ near $\omega/JS \approx 0.39$. Another example of this behavior is given in figure 8.19, for index $m = 16$ which gives $\mathbf{q} = (\pi/4, 0)$. In this case the CP that appears in $S^{xx}(\mathbf{q}, \omega)$ for $\tilde{T} > \tilde{T}_c$ is wider than that at lower wave vector. Again, the spin wave peak is easily identified in $S^{zz}(\mathbf{q}, \omega)$, although it has a long tail down to zero frequency for $\tilde{T} > \tilde{T}_c$.

8.7.4 Ideal gas model for vortex thermodynamics

Intensity in the dynamic correlations at low frequency and low wave vector is due to larger or extended objects with slow motions. Although spin waves are extended objects, they possess a well-defined $\mathbf{q}$ and we know that their dynamic response at finite temperature is mainly a softened and broadened peak at a reduced spin wave frequency. We have seen that the CP in $S^{xx}(\mathbf{q}, \omega)$ appears only as the temperature surpasses T_c, where we know that a considerable density of vortices and anti-vortices has been generated. The spin waves are still visible in $S^{zz}(\mathbf{q}, \omega)$ for $T > T_c$. Vortices generally have extended in-plane spin profiles, and can be excited with slow velocities, which suggests that they should produce in-plane CP intensity. They may also produce a weaker out-of-plane CP, due to the out-of-plane spin structure in moving vortices. Of course, if only slowly moving vortices are present, then they can produce only small S^z spin components, and small contributions to $S^{zz}(\mathbf{q}, \omega)$. These facts suggest that thermally generated vortices in the BKT transition are primarily

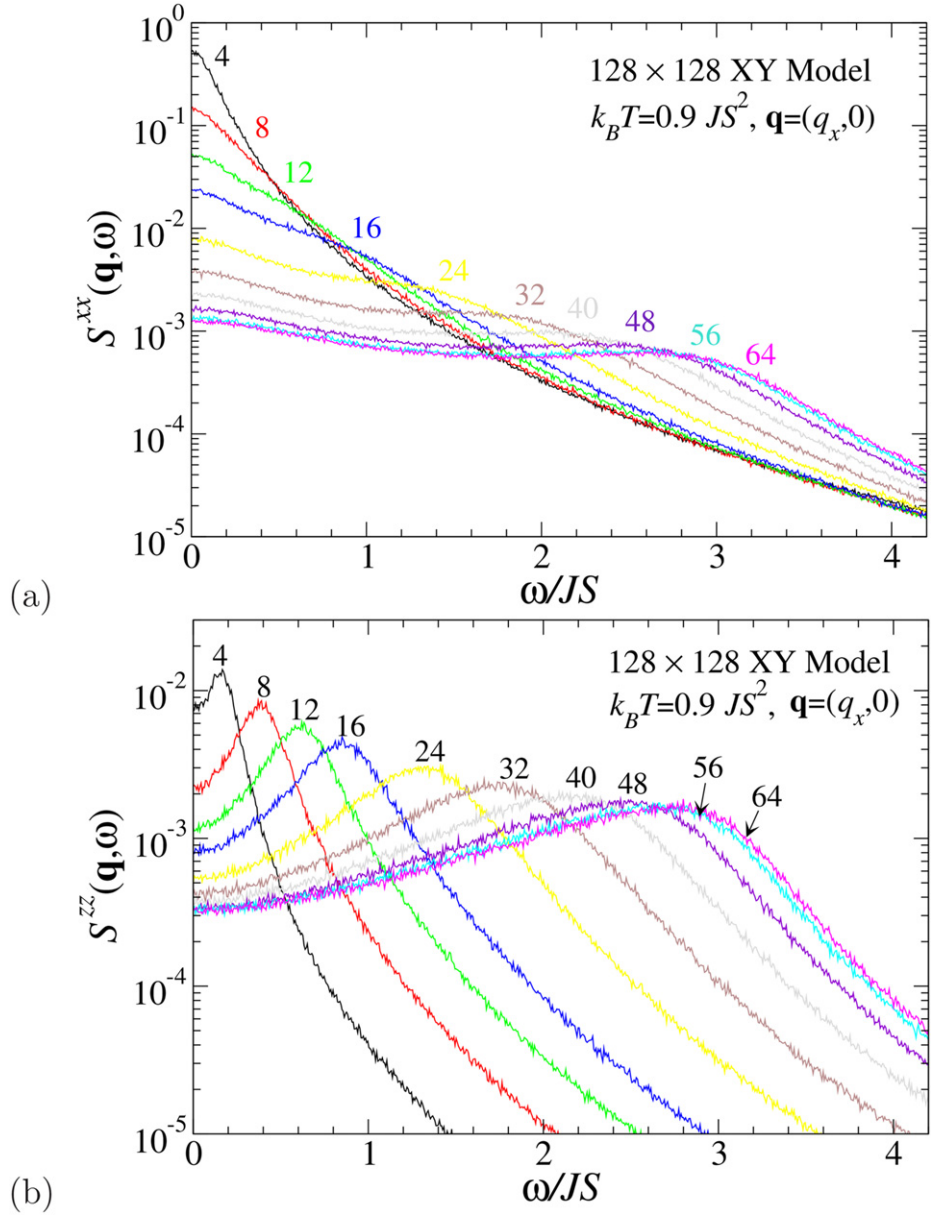

Figure 8.17. Dynamic structure functions (a) in-plane, $S^{xx}(\mathbf{q}, \omega)$ and (b) out-of-plane, $S^{zz}(\mathbf{q}, \omega)$, for the square lattice FM XY model ($L = 128$, $\lambda = 0$) at $k_B T = 0.9JS^2$, from averages over 500 initial conditions, with each $q_x = 2\pi m/L$ for indicated m values. In (a) the colors on m values are used to indicate the corresponding curves. The in-plane correlations now are dominated by the CP signature of vortices. The spin wave peaks are weakened, greatly broadened and mainly visible only in the out-of-plane correlations.

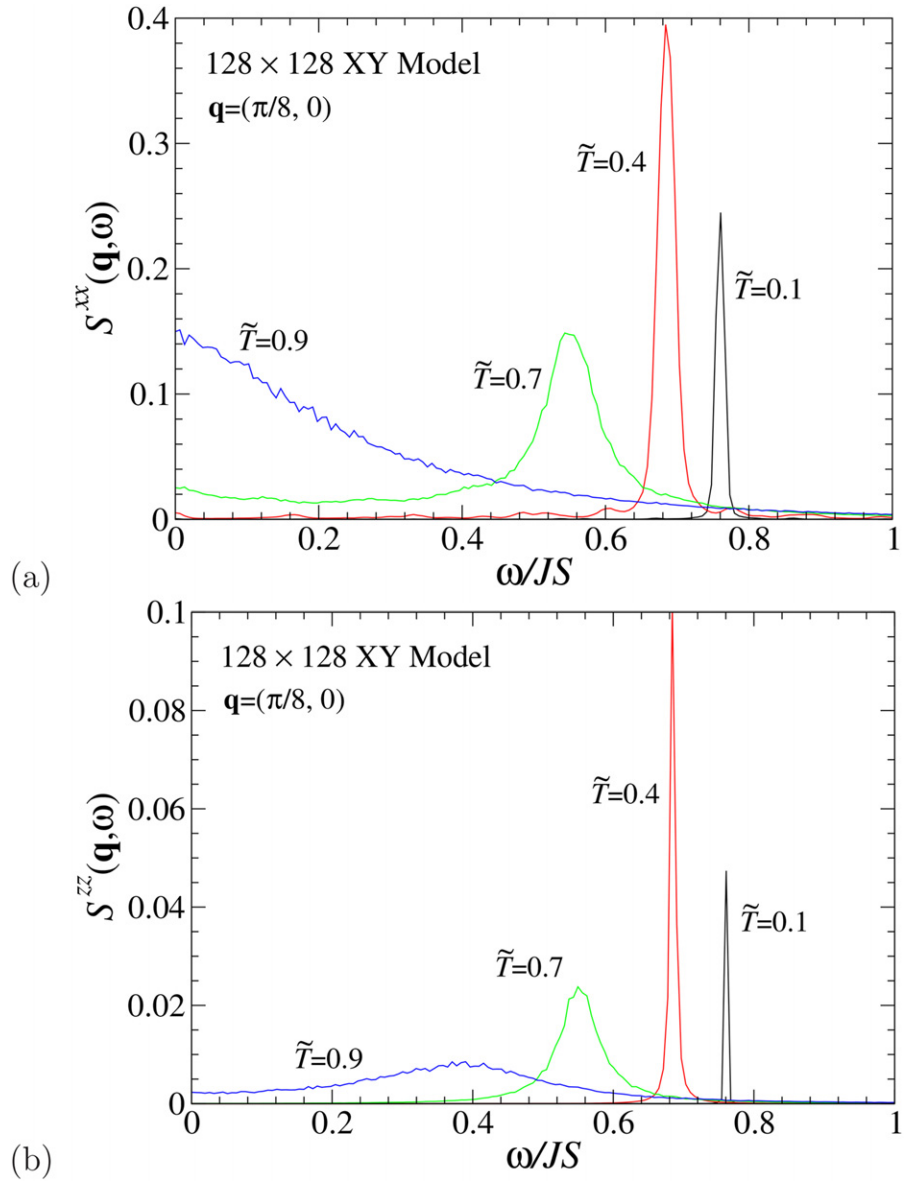

Figure 8.18. Dynamic structure functions for the square lattice FM XY model ($L = 128$, $\lambda = 0$) at $\mathbf{q} = (\pi/8, 0)$, corresponding to wave vector index $m = 8$ in figure 8.17, (a) in-plane, $S^{xx}(\mathbf{q}, \omega)$, and (b) out-of-plane, $S^{zz}(\mathbf{q}, \omega)$, for indicated temperatures $\tilde{T} = k_B T/JS^2$. Note the growth of the CP for $\tilde{T} > \tilde{T}_c \approx 0.7$, and how the spin wave peak is more visible in the out-of-plane correlations at $\tilde{T} = 0.9$.

responsible for the CP in $S^{xx}(\mathbf{q}, \omega)$, and they may make some minor contributions to $S^{zz}(\mathbf{q}, \omega)$ at low frequencies.

These ideas inspired an analysis by Mertens *et al* [25] in terms of an 'ideal gas' of vortices moving in a background of spin waves, which is similar to a model for an

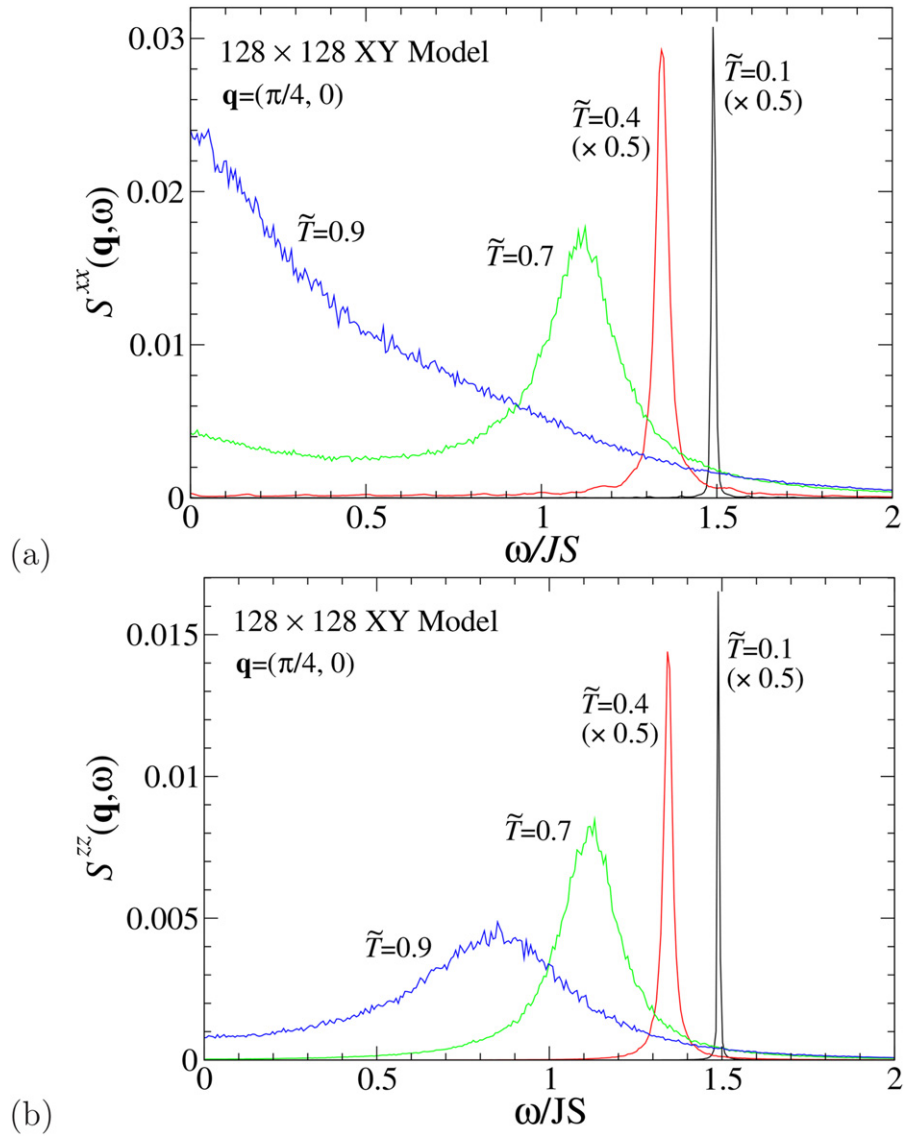

Figure 8.19. Dynamic structure functions for the square lattice FM XY model ($L = 128$, $\lambda = 0$) at $\mathbf{q} = (\pi/4, 0)$, corresponding to wave vector index $m = 16$ in figure 8.17, (a) in-plane, $S^{xx}(\mathbf{q}, \omega)$, and (b) out-of-plane, $S^{zz}(\mathbf{q}, \omega)$, for indicated temperatures $\tilde{T} = k_B T/JS^2$.

ideal gas of solitons in quasi-1D magnetic chains. Here we describe some aspects of this ideal gas model. It can be kept in mind that it makes some assumptions which may not be exactly correct. Further, it is possible to consider other processes that could lead to CP intensity, such as multi-spin wave interference. The main result of the ideal vortex gas model is a prediction of the vortex contribution to the width and height (or total integrated intensity) of the CPs in $S^{xx}(\mathbf{q}, \omega)$ and $S^{zz}(\mathbf{q}, \omega)$.

The basic assumptions of the ideal gas are as follows. We consider primarily $\lambda < \lambda_c$, so the vortices are of the in-plane type. For the in-plane correlations, a vortex at some point causes a reversal of the sign of in-plane spin components on either side of itself. This can be assumed to be the main way in which the correlation functions are affected and, as a result, the density of free vortices (including anti-vortices) ρ has been taken to be related to the correlation length,

$$\rho \approx (2\xi)^{-2}. \tag{8.72}$$

This can be viewed to say that the correlation length ξ is half the mean vortex separation, $\rho^{-1/2}$. Note that ξ enters into the decay of in-plane correlations via (8.56). Concerning the time-dependent effects, the *free vortices* are assumed to move in a ballistic manner at constant velocity, and their population is assumed to be taken from a Maxwellian velocity distribution. These two assumptions may be the most easily called into question, because at the temperatures where many vortices are present, there are likely to be strong vortex–vortex and vortex–spin wave interactions. Any ideal gas approximation usually assumes a low density of particles, so that interactions only help with the accomplishment of ergodicity. This is probably violated for vortices in easy-plane magnets. However, we assume that the temperature is just slightly above T_c, where the lowest number density is present. In addition to this, vortices are not particles of indefinite lifetime, which is another reason that the model can be called into question. Even so, it is interesting to evaluate its predictions.

Here is a synopsis of the calculation of the dynamic correlation function as caused by ballistically moving vortices. See [25] for further details. Consider a simplified definition of the correlations of one in-plane spin component, in continuum notation for unit spins,

$$S^{xx}(\mathbf{r}, t) = \left\langle s^x(\mathbf{r}, t) s^x(\mathbf{0}, 0) \right\rangle. \tag{8.73}$$

For an individual vortex with in-plane angle given by (8.7), the spin component is $s^x = \cos\phi(\mathbf{r}, t)$. The vortex field for the in-plane spin components extends over the whole system. For two widely separated points in space with initially correlated or aligned spins, a vortex placed between them will cause a relative sign of -1 in the spin components at those points. Thus, the generation of vortices between two points leads to a *reduction* of their correlations. Then, the calculation of this correlation function requires a type of counting of the number of vortices passing between the two space–time locations. Therefore it is reduced to the form,

$$S^{xx}(\mathbf{r}, t) = \langle \cos^2 \phi(\mathbf{0}, 0) \rangle \left\langle (-1)^{N(\mathbf{r},t)} \right\rangle, \tag{8.74}$$

where $N(\mathbf{r}, t)$ counts the number of vortices passing a contour between $(\mathbf{0}, 0)$ and $(\mathbf{r}, t)$. The angle at the initial point, $\phi(\mathbf{0}, 0)$, is uniformly distributed on $[0, 2\pi]$, so that $\langle \cos^2 \phi(\mathbf{0}, 0) \rangle = 1/2$.

The other part involving the average of $(-1)^{N(\mathbf{r},t)}$ has appeared in thermal averages for 1D soliton models. Mertens *et al* [25] found a way to evaluate it analytically in two space dimensions. They considered first a 1D calculation, with

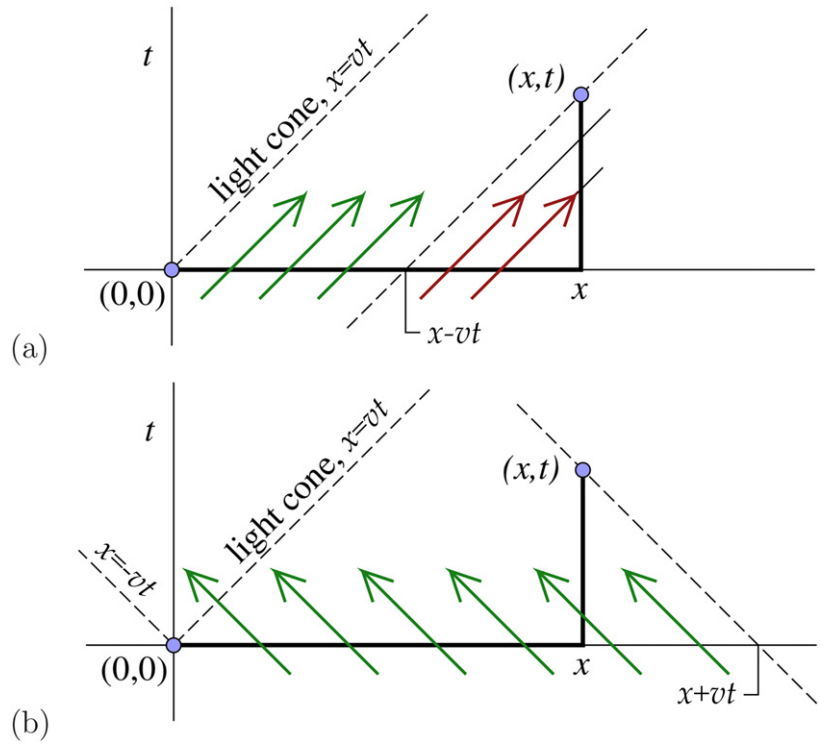

Figure 8.20. Diagram of the 'light cone' for correlations between points (0, 0) and (x, t) by calculation of the number of 1D kinks crossing the connecting contour. Point (x, t) is considered outside the light cone here. (a) For right-moving kinks of speed v, green (red) arrows show those crossing once (twice), which are counted (or not). The width that contributes is $x - vt$, which determines $\bar{n}_r$ in (8.75). (b) For left-moving kinks of speed v, all those over the width $x + vt$ cross the contour once and are counted, which determines $\bar{n}_l$ in (8.78).

kinks (instead of a vortices) of equal speeds v observed to pass the contour (0, 0) → (x, 0) → (x, t). The counting of N requires doing two cases, $x > vt$ and $x < vt$, separately. In the first case with $x > vt$, the point (x, t) is said to be *outside the light cone* (where the light cone has $x = vt$). This case is sketched in figure 8.20. In fact, we only need to consider the right-moving kinks (velocity $+v$) separately from the left-moving kinks (velocity $-v$). Later, we sum over the effects of all distinct velocities, and here $+v$ and $-v$ are themselves distinct.

In figure 8.20(a), the kinks in a region of width $x - vt$ cross the contour once and are counted (green arrows); there are also other kinks that cross twice (red arrows) so effectively they did not cross and need not be counted (or, they contribute $(-1)^2$, which makes no difference). Assuming a linear density of kinks as $\rho = (2\xi)^{-1}$, with half moving to the right and half moving to the left, the mean number of kinks to cross to the right is

$$\bar{n}_{\mathrm{r}} = \frac{1}{2}\rho(x - vt) = \frac{x - vt}{4\xi}. \tag{8.75}$$

Because a low density is assumed in ideal gas theory, the fluctuating number n_r follows a Poisson distribution,

$$p(n_r) = \frac{\bar{n}_r}{n_r!} e^{-\bar{n}_r}, \quad n_r = 0, 1, 2, \ldots. \tag{8.76}$$

Then the average needed for the right-moving kinks is calculated from

$$\left\langle (-1)^{n_r} \right\rangle = \sum_{n_r} (-1)^{n_r} p(n_r) = e^{-2\bar{n}_r} = \exp\left[-\frac{(x - vt)}{2\xi} \right]. \tag{8.77}$$

A similar calculation is applied for the left-moving kinks, see figure 8.20(b), where kinks in the width $x + vt$ all cross the contour and are counted. With n_l being the number crossing to the left, and mean value,

$$\bar{n}_l = \frac{1}{2}\rho(x + vt) = \frac{x + vt}{4\xi} \tag{8.78}$$

their contribution to the average is a similar result,

$$\left\langle (-1)^{n_l} \right\rangle = \sum_{n_l} (-1)^{n_l} p(n_l) = e^{-2\bar{n}_l} = \exp\left[-\frac{(x + vt)}{2\xi} \right]. \tag{8.79}$$

These factors combine into one factor for all kinks. When the calculations are repeated for points (x, t) also inside the light cone, the net result for an arbitrary point (x, t) inside or outside the light cone can be written as

$$\left\langle (-1)^{N(x,t)} \right\rangle = \exp\left[-\frac{|x - vt|}{2\xi} - \frac{|x + vt|}{2\xi} \right]. \tag{8.80}$$

The above calculations apply to a 1D system, but we have a 2D system and vortices, not kinks, with many different velocities. The 1D results were generalized to the 2D situation, which produces a sum over the velocity distribution:

$$\left\langle (-1)^{N(\mathbf{r},t)} \right\rangle = \exp\left[-\int_0^\infty dv\ P(v) \left[\frac{|r - vt|}{2\xi} + \frac{|r + vt|}{2\xi} \right] \right]. \tag{8.81}$$

The Maxwellian speed distribution $P(v)$, giving the same weight to inward-moving and outward-moving vortices, is

$$P(v) = 2\frac{v}{\bar{v}^2} e^{-v^2/\bar{v}^2}. \tag{8.82}$$

Of course, this is where one assumes freely moving vortices in thermal equilibrium, which implies that the root-mean-square speed $\bar{v}$ is dependent on the temperature. Integration over speeds can be shown to lead to the space–time correlation function in the form,

$$S^{xx}(\mathbf{r}, t) = \frac{1}{2} \exp\left[-\frac{r}{\xi} - \frac{\sqrt{\pi}\bar{v}|t|}{2\xi} \operatorname{erfc}\left(\frac{r}{\bar{v}|t|} \right) \right]. \tag{8.83}$$

It turns out that this can be very well approximated by another analytic expression that preserves both its integrated intensity and asymptotic behaviors as $r \to \infty$ and $t \to \infty$,

$$S^{xx}(\mathbf{r}, t) \approx \frac{1}{2} \exp\left(-\sqrt{(r/\xi)^2 + (\gamma t)^2}\right) \tag{8.84}$$

where γ is a frequency-like quantity,

$$\gamma = \frac{\sqrt{\pi}\bar{v}}{2\xi}. \tag{8.85}$$

One can see that γ sets a time scale for vortex motion in the same way that the correlation length ξ sets a typical length scale. The space and time structures of this approximated correlation function are essentially very similar. This allows one to find the space–time FT. The result is a *squared Lorentzian form*,

$$S^{xx}(\mathbf{q}, \omega) = \frac{1}{2\pi^2} \frac{\gamma^3 \xi^2}{\left\{\omega^2 + \gamma^2\left[1 + (q\xi)^2\right]\right\}^2}. \tag{8.86}$$

In fact, this is indeed a CP structure; the maximum intensity occurs at $\omega = 0$. The height of the CP as a function of $\mathbf{q}$ is one quantity that can be analyzed. The ideal gas model then predicts it to be

$$S^{xx}(\mathbf{q}, \omega = 0) = \frac{1}{2\pi^2} \frac{\gamma^{-1}\xi^2}{\left[1 + (q\xi)^2\right]^2} = \frac{A}{\left[1 + (q\xi)^2\right]^p}, \quad p = 2. \tag{8.87}$$

The amplitude $A = S^{xx}(\mathbf{q} = \mathbf{0}, \omega = 0)$ will be taken from the MC–SD data. The power $p = 2$ comes from the ballistic ideal gas theory, but we allow for a different power in the expression for later analysis. The CP also has a $\mathbf{q}$-dependent half-width, defined as the frequency where $S^{xx}(\mathbf{q}, \omega)$ reaches half its peak value, which is found to be

$$\Gamma_x(\mathbf{q}) = \left(\sqrt{2} - 1\right)^{1/2} \gamma\left[1 + (q\xi)^2\right]^{1/2} = B\left[1 + (q\xi)^2\right]^{1/2} \tag{8.88}$$

Again, its scale or amplitude is determined by the constant $B = \Gamma_x(\mathbf{q} = \mathbf{0})$, which can be taken from MC–SD data. The total intensity integrated over all frequency (assuming symmetry in positive and negative ω) is

$$I_x(\mathbf{q}) = \int_{-\infty}^{+\infty} \mathrm{d}\omega\ S^{xx}(\mathbf{q}, \omega) = \frac{1}{4\pi} \frac{\xi^2}{\left[1 + (q\xi)^2\right]^{3/2}} = \frac{C}{\left[1 + (q\xi)^2\right]^{p-1/2}}, \quad p = 2. \tag{8.89}$$

Its scale is the constant $C = I_x(\mathbf{q} = \mathbf{0})$. These last three equations can be tested by comparison with the MC–SD simulations. The values at $\mathbf{q} = \mathbf{0}$ are factored out, which facilitates comparison with simulation or experiment, and allows one to concentrate more on the dependencies with $\mathbf{q}$. This is helpful because it is difficult for theory to correctly obtain the amplitude of the CP effects, because indeed other processes besides vortex motion can be responsible for some of the intensity. Note that the

vortex ideal gas CP intensity is predicted to vary as $\xi^2 \sim \rho^{-1}$ for small wave vectors, which is physically reasonable. The vortices generated thermally as T increases above T_c reduce the long-distance correlations across the system. The predicted CP half-width is only weakly dependent on q for small q (long wavelengths), and eventually approaches an approximate linear relation with q at larger values.

8.7.5 Comparison of vortex ideal gas model to simulations

Mertens *et al* [25] originally made various comparisons of these ideal gas predictions with early simulation data by averaging over only three initial states, and found reasonably good agreement for the **q**-dependencies, but not so much so for the amplitude of the effects. For comparison here we show some additional results on 128×128 systems for just one temperature, $k_B T = 0.9JS^2$, slightly above T_c, averaging over 500 initial states. At this temperature, $\rho \approx 0.094$, which would imply by (8.72) a correlation length on the order of $\xi \approx 1.63a$, however, that is probably an underestimate. The alternative relation,

$$\rho \approx \xi^{-2} \tag{8.90}$$

gives instead $\xi \approx 3.26a$, which is more consistent with results from static correlations. Indeed, Dimitrov and Wysin [26] found $\xi = 3.95a$ at this temperature from the static correlation function. In addition, they show in figure 1 of [26] that the relation between vortex number density and ξ^{-2} is not even linear.

For the full range of wave vectors along the (10)-direction, the CP height for $S^{xx}(\mathbf{q}, \omega)$ was measured (at $\omega = 0$); results are shown in figure 8.21. The frequency at which $S^{xx}(\mathbf{q}, \omega)$ becomes half the height was used to estimate the half-width Γ_x, which is plotted in figure 8.22. Then, based on the theory expressions for the squared Lorentzian CP, one finds that the height and half-width can be combined directly to estimate the integrated intensity,

$$I_x(\mathbf{q}) = \frac{\pi}{2}\left(\sqrt{2} - 1\right)^{-1/2} S^{xx}(\mathbf{q}, \omega = 0)\, \Gamma_x(\mathbf{q}) \approx 2.44\, S^{xx}(\mathbf{q}, \omega = 0)\, \Gamma_x(\mathbf{q}). \tag{8.91}$$

The intensity from the simulations is then a derived quantity calculated this way from the estimates of CP height and half-width, see figure 8.23. This also means that the amplitudes (values at $\mathbf{q} = \mathbf{0}$) are related by

$$C = \approx 2.44AB. \tag{8.92}$$

In order to compare simulation data with the theory, the values of CP height, half-width and intensity at $\mathbf{q} = 0$ were taken directly from the simulations, and not allowed to be fitted. These values from the simulations give the constants in dimensionless units, $A = 1.26$, $B = 0.087$ and $C = 2.44AB = 0.268$. One can note that the implied definition of $C = \xi^2/4\pi$ results in the estimate of correlation length, $\xi = 1.83a$. On the other hand, if the alternative definition (8.90) were used in the ideal gas model, the result would instead be $\xi \approx 3.66a$, which is more reasonable and close to that from static correlations [26].

Figure 8.21 shows the MC–SD data for CP height compared with the ideal gas theory expression (8.87), at the power $p = 2$ and also for an alternative value

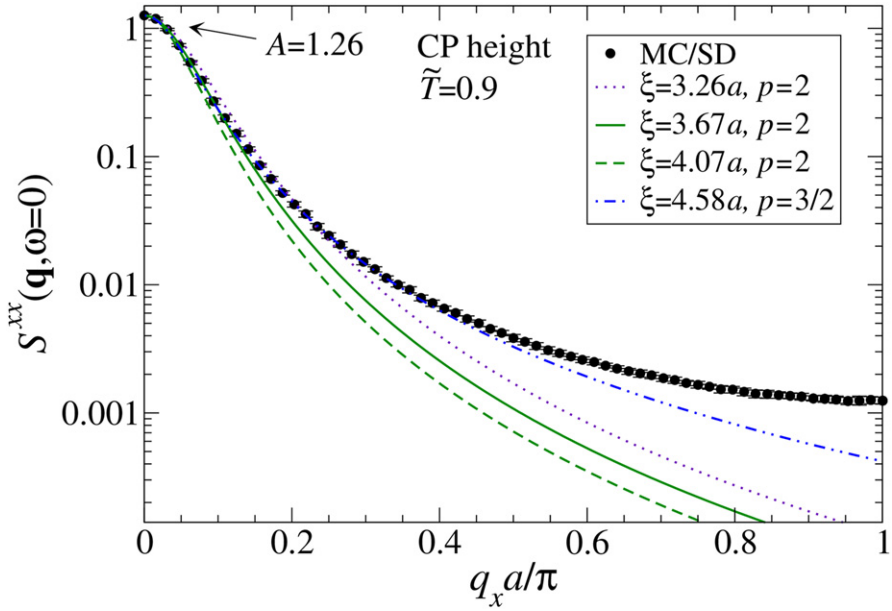

Figure 8.21. CP height at $\tilde{T} = 0.9$ for wave vectors $\mathbf{q} = (q_x, 0)$ on the 128×128 FM XY model system. Symbols are from the hybrid MC–SD simulations. Curves are the ideal gas expression (8.87), using the different values of ξ indicated. The power $p = 2$ is the ballistic ideal gas model; for power $p = 3/2$, however, the data can be fit over a much wider range of q_x.

$p = 3/2$. The theory expression with $p = 2$, $\xi = 3.67a$ fits well to the simulations at low q, but deviates significantly with increasing q. Other values of ξ are shown for comparison. It was noticed that putting $p = 3/2$ allows for a much better fit to large q, using $\xi = 4.58a$. However, the simulation data go to a constant height at the zone boundary, whereas the theory expression continues decaying.

Figure 8.22 shows the MC–SD data for CP half-width $\Gamma_x(\mathbf{q})$ compared with the ideal gas theory, equation (8.88). A value of $\xi = 6.11a$ gives a good match at low q; it seems that there is a change in the slope of $\Gamma_x(\mathbf{q})$ around $q_x \approx 0.32\pi/a$. A value of $\xi = 5.50a$ gives a better fit over the full range of q. Trial curves with smaller values of ξ such as $\xi = 3.67a$ fail to follow the MC–SD data.

Figure 8.23 shows the MC–SD data for CP intensity $I_x(\mathbf{q})$, from using (8.91), compared with the ideal gas theory, (8.89). Various values of ξ for the ballistic theory $p = 2$ can only fit to the data at lower q; the best is around $\xi = 3.67a$. Similar to the peak height, the integrated intensity seems to be better fit over a wider range of q by switching to the power $p = 3/2$, for which $\xi = 3.97a$ gives a good fit. Eventually at large enough q, the MC–SD tends to a constant, then the theoretical expression (8.89) cannot follow the data.

These results indicate that the vortex ideal gas theory does predict a CP, and while the gross features are present, probably the details do not work out completely correctly. It is difficult to obtain all three of the main quantities, peak height, peak width and integrated intensity, to match to the theory with the same correlation

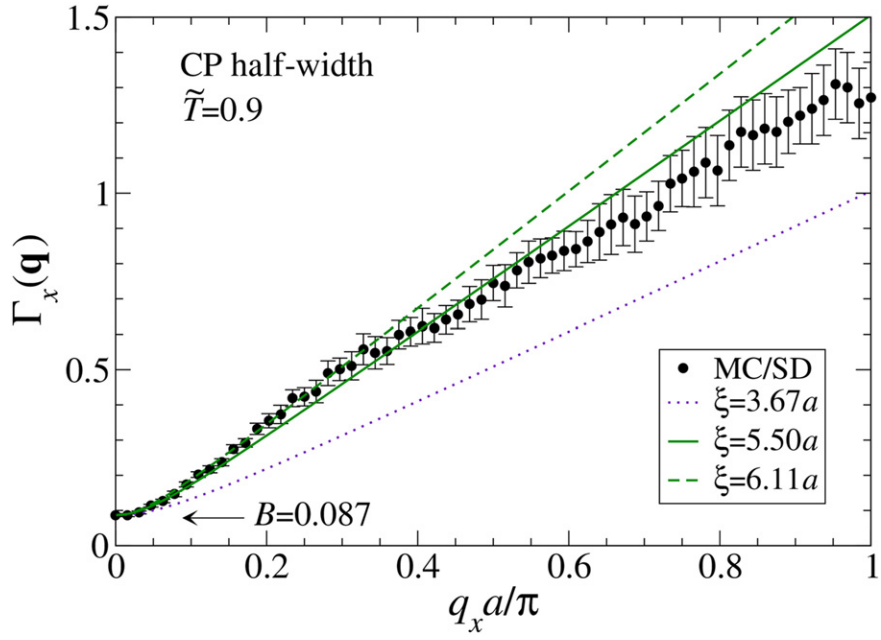

Figure 8.22. CP half-width at $\tilde{T} = 0.9$ for wave vectors $\mathbf{q} = (q_x, 0)$ on the 128×128 FM XY model system. Symbols are from the hybrid MC–SD simulations. Curves are the ideal gas expression (8.88), using the different values of ξ indicated. Note that the value $\xi = 6.11a$ fits well at low q_x, where the spin wave peak in $S^{xx}(\mathbf{q}, \omega)$ is very weak.

length parameter ξ. It is also possible that the structure of $S^{xx}(\mathbf{q}, \omega)$ is not so close to a squared Lorentzian, as indicated that the peak height might better be fit with the power $p = 3/2$ instead of $p = 2$ as in the ideal gas theory. The amplitudes of these quantities were fixed to the simulation results, because they could not be consistently matched, to give one good set of values for ξ and γ. Even so, the idea of slow-moving vortices and the sign-change in a vortex, that causes a contribution to the dynamic correlations, is completely reasonable as an explanation of the vortex part of CP intensity.

We have noted that the theory presumes relation (8.72) between vortex density and correlation length, however, an alternative relation (8.90) without the factor of 2 could be one improvement. In any case, the vortex density is not really linearly proportional to ξ^{-2} [26], as assumed. As mentioned earlier, another probable correction to the results is to take into account the spin wave and multi-spin wave interference contributions, because these also contribute to CP intensity. At higher T and higher vortex density, the ideal gas assumption will become invalid. The process itself of VA pair creation has been proposed as making a contribution to CP intensity [27], especially below T_c [28]. In addition to these effects, other simulations indicate that vortices have significantly finite lifetimes [26]. This is certainly an effect that is mixed up with the scattering of spin waves off vortices and spin waves off other spin waves. This means that the ballistic approximation is probably not as

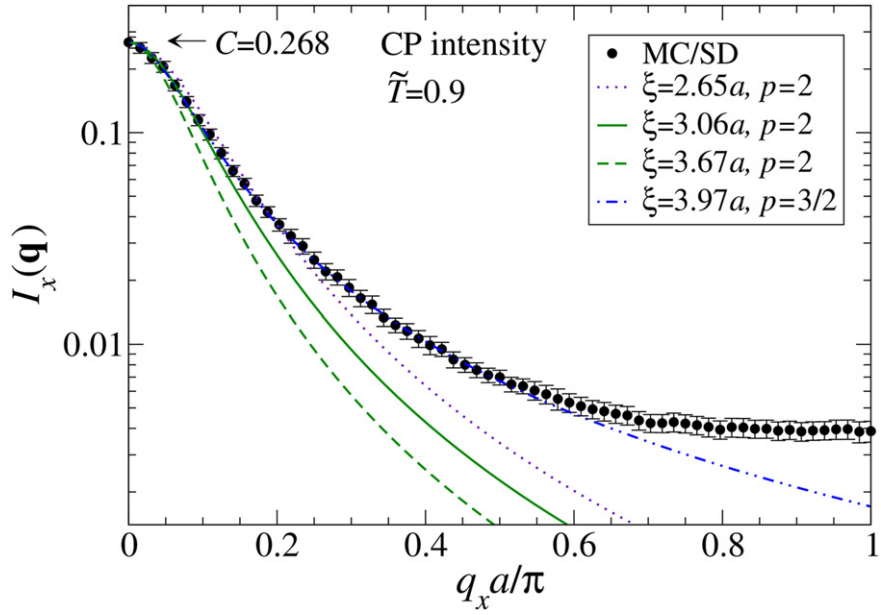

Figure 8.23. CP integrated intensity at $\tilde{T} = 0.9$ for wave vectors $\mathbf{q} = (q_x, 0)$ on the 128×128 FM XY model system. Symbols are from the hybrid MC–SD simulations. Curves are the ideal gas expression (8.89), using the different values of ξ indicated. The power $p = 2$ is the ballistic ideal gas model; for power $p = 3/2$, however, the data can be fit over a much wider range of q_x.

good as it should be, as finite lifetime will lead to a lower frequency limit below which the vortex ideal gas theory needs modification.

The theory was extended also to apply to out-of-plane correlations $S^{zz}(\mathbf{q}, \omega)$, however, this depends strongly on the true structure of moving vortices. Mertens *et al* [25] again found a CP, but of Gaussian form. For interested readers further discussion of that can be found in the literature.

8.7.6 Dynamic correlations with vacancies

Earlier we saw how spin vacancies lead to a reduction of T_c in the XY model, as shown through calculations of the helicity modulus and static correlations. Vacancies tend to attract and pin vortices, even for temperatures below T_c. It has been seen [22] that most of the vortices produced below T_c are in fact, pinned on vacancies. Then, it is interesting to ask if there is a dynamic signature due to pinned vortices, that appears in the dynamic structure function. A vortex pinned on a vacancy has lowered its energy by doing so. It is in a local potential energy minimum, then, it possesses certain dynamic modes of oscillation about its minimum, which should present themselves in $S^{xx}(\mathbf{q}, \omega)$.

In a paper [29] by Paula *et al* this question was addressed by making MC–SD simulations for the XY model with a percentage of randomly placed vacancies. They

found that for temperatures below the critical temperature (for a given density of vacancies), there appears in $S^{xx}(\mathbf{q}, \omega)$ not only the spin wave peak, but as well an extra small peak at a low frequency inversely proportional to the lattice size L. This could be typical of finite size effects. However, the frequency found for the mode seems to match that expected for the normal mode oscillations for a pinned vortex, as calculated analytically and by simulations [20]. At $T = 0$ the prediction is for the frequency of a single vortex on a single vacancy in a $L \times L$ system is predicted to be

$$\omega_0 = \frac{13.57}{L} JS. \tag{8.93}$$

When considering higher temperature, the frequency of this type of mode is expected to soften due to thermal effects. Softening is also involved with increasing vacancy density, which weakens the average exchange couplings and therefore lowers the frequencies, see figure 3 of [29].

As an example of these effects, here we show some results from MC–SD simulations with a vacancy density $\rho_{\text{vac}} = 0.16$, for the 128×128 XY model, see figure 8.24. For reference, simulation results for the same pure system, without vacancies, are shown in figure 8.25. The averages have been made over 500 states of the ensemble, including averaging over the random vacancy locations. This was

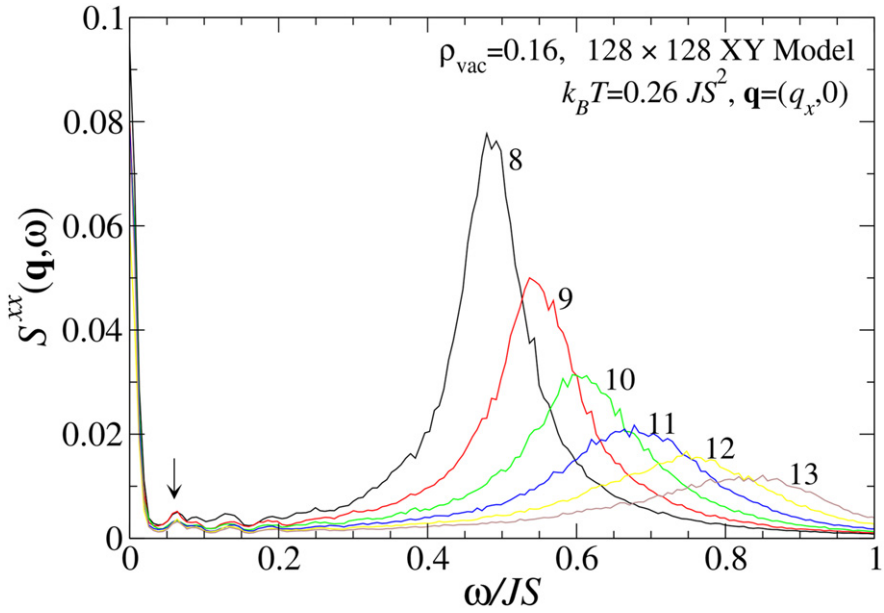

Figure 8.24. In-plane dynamic correlations in the presence of 16% vacancies on the 128×128 FM XY model system, from MC–SD simulations, for wave vectors $\mathbf{q} = (m, 0)(2\pi/L)$ with m values indicated next to the curves. The temperature $k_B T = 0.26JS^2$ is about 4/7 of T_c. The arrow at $\omega/JS \approx 0.064$ indicates a mode likely due to vortices pinned on vacancies, whose frequency does not change with $\mathbf{q}$. Note that the peak also is present no matter whether m is odd or even. There is also a very strong peak at $\omega = 0$ for all the $\mathbf{q}$ shown, caused by the vacancy disorder; compare figure 8.25.

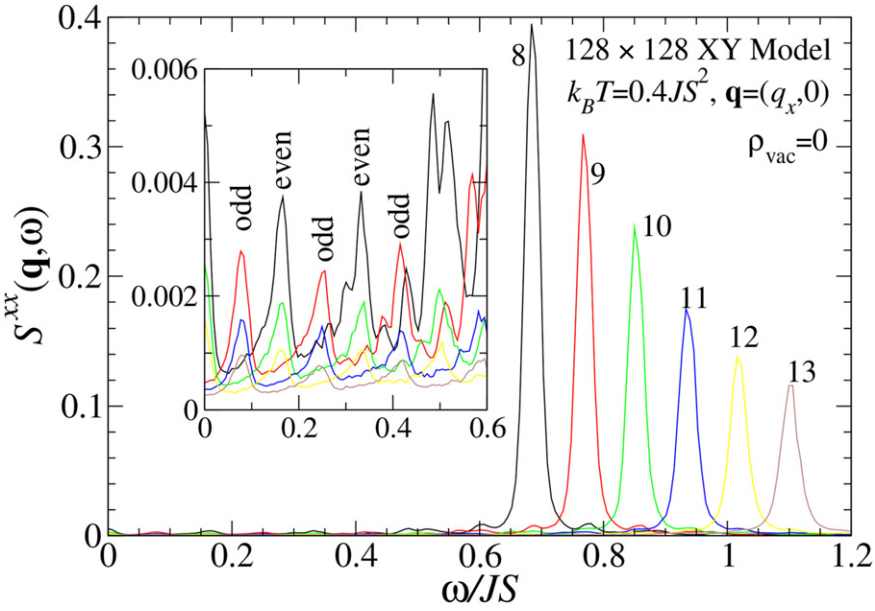

Figure 8.25. In-plane dynamic correlations in the pure 128 × 128 FM XY model system (no vacancies), from MC–SD simulations, for wave vectors $\mathbf{q} = (m, 0)(2\pi/L)$ with m values indicated next to the curves. The temperature is about 4/7 of T_c. The inset shows a zoom of the weak typical finite size responses below the spin wave peaks, that depend on whether m is odd or even.

achieved by making 25 realizations of the vacancy positions, from which the MC simulations were run to 20 000 MCS for equilibration, and then run another 20 000 MCS, taking a state to be an initial condition for the SD every 1000 MCS. The SD part of the simulations was run the same way as described earlier for the XY model, using $2^{12} = 4096$ time points separated by $\Delta t = 6 \times 0.04(JS)^{-1}$. At a 16% vacancy density, the transition temperature is $k_BT_c \approx 0.453JS^2$, see figure 8.12. Due to the lower T_c compared to $k_BT_c \approx 0.70JS^2$ in the pure model, we consider the simulations at relatively lower temperatures. So we show results at $k_BT \approx (4/7)k_BT_c = 0.26JS^2$ and at $T \approx T_c$.

Referring to figure 8.24 for $T \approx (4/7)T_c$ with 16% vacancies, the spin wave peak is the dominant feature, moving in frequency as the wave vector is changed. However, also a very strong peak appears at $\omega = 0$ for any $\mathbf{q}$. Such a peak at zero frequency of course belies the presence of a frozen-in spin structure. This feature has not been carefully analyzed, but it is certainly caused by the vacancies and the fact that the thermal averages of total S^x and S^y are now not zero when vacancies are present. The vacancies break the full symmetry of the system. The exchange interactions where sites do not all have four nearest neighbors must produce a frozen-in organized spin structure. Note that in figure 8.25 for the corresponding wave vectors in the pure system, naturally there is no zero-frequency peak.

The second obvious feature in figure 8.24 that is directly caused by the presence of vacancies is the weak peak at a low frequency of about $\omega \approx 0.064JS$, indicated by an

arrow. That feature and some other similar small peaks remain present for all the **q** shown. Paula *et al* [29] have indicated that this small feature is ultimately caused by the oscillations of vortices pinned on vacancies. The frequency is quite low compared to the $T = 0$ prediction from (8.93), which gives $\omega_0 \approx 0.106JS$, however, the vacancies distributed over the system weaken the average exchange interactions, which causes a considerable lowering of this mode's frequency. The values of m used to produce the wave vectors, according to $q_x = 2\pi m/L$, are both odd and even, and yet the low frequency features remain nearly the same. Compare the inset in figure 8.25 for the pure system, which shows the very weak response below the spin wave frequency. In the pure system these low frequency peaks alternate by odd/even values of m, which is typical for finite size spin wave effects. This gives a strong indication that the small low frequency structures in the system with vacancies really are due not to spin wave effects, but to pinned vortices.

It is interesting to make another comparison for the same system, with (figure 8.26) and without (figure 8.27) vacancies, but at a temperature more or less equal to T_c. In the system with vacancies, the spin waves are broadened, and there starts to appear a general wide background similar to a CP. The narrow peak at $\omega = 0$ is still present. There is also a very faint but broadened possible peak around $\omega \approx 0.055JS$, that is probably the pinned vortex oscillation. It has been both broadened and

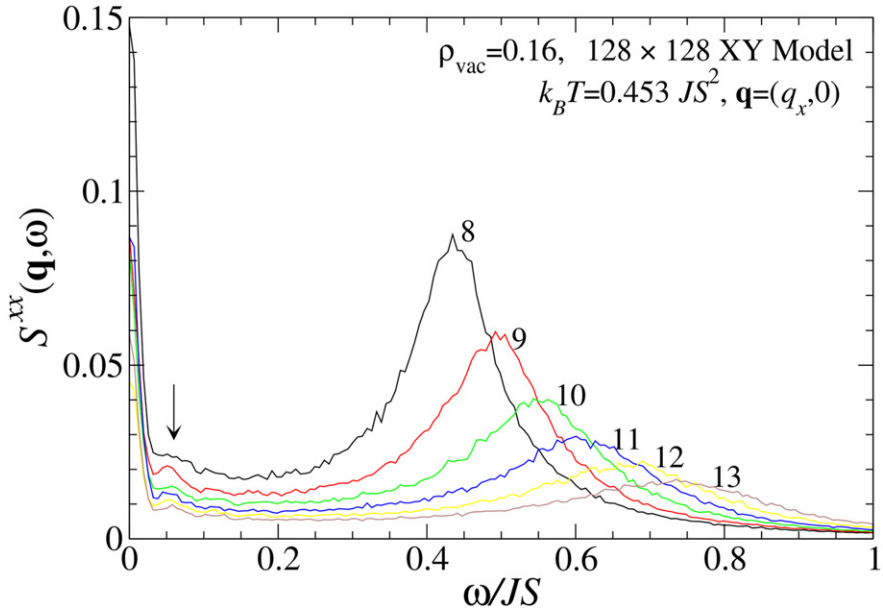

Figure 8.26. In-plane dynamic correlations in the presence of 16% vacancies on the 128 × 128 FM XY model system, from MC–SD simulations, for wave vectors $\mathbf{q} = (m, 0)(2\pi/L)$ with m values indicated next to the curves. The temperature is the critical temperature. The arrow at $\omega/JS \approx 0.055$ indicates the mode probably due to vortices pinned on vacancies, that has shifted downward with increasing temperature. Note that the peak also is present no matter whether m is odd or even. The strong narrow peak at $\omega = 0$ for all the **q** is still present, caused by the vacancy disorder; compare figure 8.27.

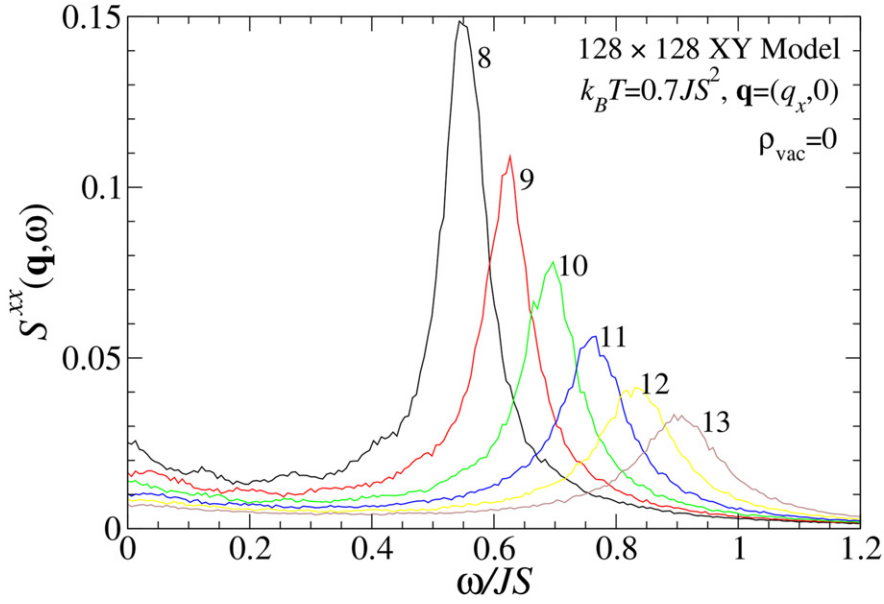

Figure 8.27. In-plane dynamic correlations in the pure 128 × 128 FM XY model system (no vacancies), from MC–SD simulations, for wave vectors $\mathbf{q} = (m, 0)(2\pi/L)$ with m values indicated next to the curves. The temperature is the critical temperature. The weak finite size responses below the spin wave peaks that depend on whether m is odd or even are still present but rather broadened, compare figure 8.25.

moved to a lower frequency compared to that in figure 8.24 for $T \approx (4/7)T_c$, due to greater thermal effects. Again this faint peak is present regardless of whether the wave vector index m is odd or even. In the system without vacancies at $T = T_c$, figure 8.27, the spin wave peaks are narrower, and there is also a general wide background, with weak oscillations. Looking more closely, the curves still exhibit a weak set of finite size effects peaks that depend on whether m is odd or even. These finite size effect peaks are rather broadened due to the temperature. But there is no single weak peak present independent of $\mathbf{q}$ such as that in the system with vacancies.

All these results taken together point to the idea that the fraction of vortices pinned on vacancies make small-amplitude oscillations. The oscillation has a particular signature, which is exhibited as a weak peak at a frequency lower than that given in the zero-temperature estimate of equation (8.93). The softening of its frequency occurs both due to increasing temperature and increasing vacancy density. Each of those effects lowers the effective exchange interaction strength, thereby reducing the mode frequency. Once the temperature is above T_c, this weak peak is gone because of the growth of the much larger CP associated with the much greater vortex density of the BKT transition.

Bibliography

[1] Hikami S and Tsuneto T 1980 Phase transition of quasi-two-dimensional planar system *Prog. Theor. Phys.* **63** 387

[2] Hirakawa K, Yoshizawa H and Ubukoshi K 1982 Neutron scattering study of the phase transition in two-dimensional planar ferromagnet K_2CuF_4 *J. Phys. Soc. Japan* **51** 2151
[3] Gouvêa M E, Wysin G M, Bishop A R and Mertens F G 1989 Vortices in the classical two-dimensional anisotropic Heisenberg model *Phys. Rev.* B **39** 11840
[4] Wysin G M, Gouvêa M E, Bishop A R and Mertens F G 1988 Classical spin dynamics in the two-dimensional anisotropic Heisenberg model In ed D P Landau, K K Mon and H B Schuttler *Computer Simulation Studies in Condensed Matter Physics: Recent Developments* vol 33 (Berlin: Springer) pp 40–8
[5] Takeno S and Homma S 1980 Classical spin systems, nonlinear evolution equations, and nonlinear excitations *Prog. Theor. Phys.* **64** 1193
[6] Nikiforov A V and Sonin É B 1983 Dynamics of magnetic vortices in a planar ferromagnet *Zh. Eksp. Teor. Fiz.* **85** 642
[7] Wysin G M 1996 Magnetic vortex mass in two-dimensional easy-plane magnets *Phys. Rev.* B **54** 15156
[8] Wysin G M 1994 Instability of in-plane vortices in two-dimensional easy-plane ferromagnets *Phys. Rev.* B **49** 8780
[9] Zaspel C E and Godinez D 1996 Vortex energies in the two-dimensional easy-plane ferromagnet *J. Magn. Magn. Mater.* **162** 91
[10] Wysin G M 1998 Critical anisotropies of two-dimensional magnetic vortices *Phys. Lett.* A **240** 95
[11] Berezinskii V L 1971 Destruction of long-range order in one-dimensional and two-dimensional systems having a continuous symmetry group I. Classical systems *Sov. Phys. JETP* **32** 493
[12] Berezinskii V L 1972 Destruction of long-range order in one-dimensional and two-dimensional systems having a continuous symmetry group II. Quantum systems *Sov. Phys. JETP* **34** 610
[13] Kosterlitz J M and Thouless D J 1973 Ordering, metastability and phase transitions in two-dimensional systems *J. Phys. C: Solid State. Phys.* **6** 1181
[14] Cuccoli A, Tognetti V and Vaia R 1995 Two-dimensional XXZ model on a square lattice: a Monte Carlo simulation *Phys. Rev.* B **52** 10221
[15] Harada K and Kawashima N 1997 Universal jump in the helicity modulus of the two-dimensional quantum XY model *Phys. Rev.* B **55** R11949
[16] Minnhagen P 1987 The two-dimensional Coulomb gas, vortex unbinding, and superfluid-superconducting films *Rev. Mod. Phys.* **59** 1001
[17] Pereira A R, Mól L A S, Leonel S A, Coura P Z and Costa B V 2003 Vortex behavior near a spin vacancy in two-dimensional XY magnets *Phys. Rev.* B **68** 132409
[18] Wysin G M 2003 Vortex-vacancy interactions in two-dimensional easy-plane magnets *Phys. Rev.* B **68** 184411
[19] Zaspel C E, McKennan C M and Snaric S R 1996 Instability of planar vortices in layered ferromagnets with nonmagnetic impurities *Phys. Rev.* B **53** 11317
[20] Pereira A R, Leonel S A, Coura P Z and Costa B V 2005 Vortex motion induced by lattice defects in two-dimensional easy-plane magnets *Phys. Rev.* B **71** 014403
[21] Paula F M, Pereira A R and Mól L A S 2004 Diluted planar ferromagnets: nonlinear excitations on a non-simply connected manifold *Phys. Lett.* A **329** 155
[22] Wysin G M 2005 Vacancy effects in an easy-plane Heisenberg model: Reduction of T_c and doubly charged vortices *Phys. Rev.* B **71** 094423
[23] Wysin G M, Pereira A R, Marques I A, Leonel S A and Coura P Z 2005 Extinction of the Berezinskii-Kosterlitz-Thouless phase transition by nonmagnetic disorder in planar symmetry spin models *Phys. Rev.* B **72** 094418

[24] Evertz H G and Landau D P 1996 Critical dynamics in the 2D classical XY-model: A spin dynamics study *Phys. Rev.* B **54** 12302
[25] Mertens F G, Bishop A R, Wysin G M and Kawabata C 1989 Dynamical correlations from mobile vortices in two-dimensional easy-plane ferromagnets *Phys. Rev.* B **39** 591
[26] Dimtrov D A and Wysin G M 1998 Free vortex and vortex-pair lifetimes in classical two-dimensional easy-plane magnets *J. Phys.: Condens. Matter* **10** 7453
[27] Costa J E R and Costa B V 1996 Static and dynamic simulation in the classical two-dimensional anisotropic Heisenberg model *Phys. Rev.* B **54** 994
[28] Pereira A R and Costa J E R 1996 Vortex pairs and central peak in the dynamic structure factor in the 2D XY model below T_{KT} *J. Magn. Magn. Mater.* **162** 219
[29] Paula F M, Pereira A R and Wysin G M 2005 Contribution of impurity-pinned vortices to the response function in a randomly diluted easy-plane ferromagnet on a square lattice *Phys. Rev.* B **72** 094425